Rock Mechanics and Rock Engineering (2024) 57:1329–1351
https://doi.org/10.1007/s00603-023-03619-2

ORIGINAL PAPER

A New Volumetric Strain-Based Method for Determining the Crack Initiation Threshold of Rocks Under Compression

Hao Li[1] · Ruizhi Zhong[2] · Leo Pel[3] · David Smeulders[1] · Zhenjiang You[2,4,5]

Received: 4 October 2022 / Accepted: 12 October 2023 / Published online: 8 November 2023

Abstract

The crack initiation stress threshold (σ_{ci}) is an essential parameter in the brittle failure process of rocks. In this paper, a volumetric strain response method (VSRM) is proposed to determine the σ_{ci} based on two new concepts, i.e., the dilatancy resistance state index (δ_{ci}) and the maximum value of the dilatancy resistance state index difference ($|\Delta\delta_{ci}|$), which represent the state of dilatancy resistance of the rock and the shear sliding resistance capacity of the crack-like pores during the compressive period, respectively. The deviatoric stress corresponding to the maximum $|\Delta\delta_{ci}|$ is taken as the σ_{ci}. We then examine the feasibility and validity of the VSRM using the experimental results. The results from the VSRM are also compared with those calculated by other strain-based methods, including the volumetric strain method (VSM), crack volumetric strain method (CVSM), lateral strain method (LSM) and lateral strain response method (LSRM). Compared with the other methods, the VSRM is effective and reduces subjectivity when determining the σ_{ci}. Finally, with the help of the proposed VSRM, influences from chemical corrosion and confining stress on the σ_{ci} and $\Delta\delta_{ci}$ of the carbonate rock are analyzed. This study provides a subjective and practical method for determining σ_{ci}. Moreover, it sheds light on the effects of confinement and chemical corrosion on σ_{ci}.

Highlights

- A volumetric strain response method (VSRM) is proposed to determine the crack initiation stress threshold from the volumetric strain curve.
- Two novel parameters, i.e., the dilatancy resistance state index and the maximum dilatancy resistance state index difference, are proposed to help the VRSM determine σ_{ci}.
- Rock's compressive stage is divided into two stages: the interlocking stage and the shear sliding stage. The crack initiation stress threshold divides these two stages.
- Relationships between the crack initiation stress threshold and rock's mechanical properties (i.e., Young's modulus, Poisson's ratio, mobilized cohesion and friction angle) are analyzed.

Keywords Crack initiation threshold · Volumetric strain · Dilatancy resistance index · Shear sliding resistance · Triaxial compression

✉ Zhenjiang You
zhenjiang.you@gmail.com

[1] Department of Mechanical Engineering, Eindhoven University of Technology, 5600 MB Eindhoven, The Netherlands

[2] Centre for Natural Gas, The University of Queensland, Brisbane, QLD 4072, Australia

[3] Department of Applied Physics, Eindhoven University of Technology, 5600 MB Eindhoven, The Netherlands

[4] Center for Sustainable Energy and Resources, Edith Cowan University, Joondalup, WA 6027, Australia

[5] School of Chemical Engineering, The University of Queensland, Brisbane, QLD 4072, Australia

1 Introduction

The deformation and final failure of engineering rocks is a progressive damage accumulation process, i.e., the initiation, propagation and coalescence of micro- and macro-cracks (Lockner 1993; Peng and Johnson 1972; Thompson et al. 2006). This damage accumulation process has been investigated by many studies over the past several decades (Bieniawski 1967a, 1968, 1967b; Brace et al. 1966; Eberhardt et al. 1998; Liu et al. 2023; Martin and Chandler 1994; Tapponnier and Brace 1976; Wong 1982; Zhang et al. 2021; Zhao et al. 2023). It is commonly acknowledged that the damage evolution process of rocks under compression (i.e., uniaxial and triaxial compressive conditions) can be characterized into several stages based on measured strain changes during experimental tests. An example of deviatoric stress ($\sigma_1 - \sigma_3$) versus strain for Jinyun limestone under conventional triaxial compression condition is given in Fig. 1. According to the early investigations of Brace et al. (1966) and Bieniawski (1967b), the damage development of the rock in Fig. 1 can be divided into five stages: compression stage, linear elastic stage, crack initiation and stable crack growth stage, crack damage and unstable crack growth stage and post-peak stage. And these five damage development stages are divided by relevant damage thresholds, i.e., the stress thresholds of crack closure (σ_{cc}), crack initiation (σ_{ci}), dilatancy boundary (or called crack damage, σ_{cd}), peak strength (σ_p) and residual strength (σ_r).

As illustrated in Fig. 1, the rock is compacted first in damage stage 1 with the closure of microcracks and pores. During this stage, the stress–strain relation is non-linear (concave upward) and the axial stiffness increases. Once most pores are closed, the linear elastic deformation occurs, and the sample enters stage 2: the linear elastic stage. After that, the rock comes to stage 3. In this stage, cracks begin to stably initiate inside the rock sample, which can be identified by the deflection point (σ_{ci}) from the deviatoric stress-volumetric strain curve. Damage stage 4 begins with the dilatancy boundary σ_{cd} (i.e., the reverse point in the volumetric strain curve) and is terminated at the peak strength point σ_p. After the σ_p, the damage process comes to the post-peak region, namely, damage stage 5.

Apart from the five-stage damage division in Fig. 1, six-stage and seven-stage damage divisions have also been proposed by researchers. By analyzing the coupled acousto-optic-mechanical (AOM) behaviors of the flawed granite and sandstone samples, a six-stage damage division is proposed. This division has five damage thresholds, i.e., the stress thresholds of crack closure, micro-crack initiation, crack initiation, crack damage and peak strength (Zhang and Zhou 2022; Zhou and Zhang 2021; Zhou et al. 2019). Eberhardt et al. (1998) divided the damage evolution of hard rock into seven stages based on the combined use of acoustic emission technology and moving point regression. Compared with the five damage stages shown in Fig. 1, two more stress thresholds are recognized, i.e., the stress thresholds of secondary crack nucleation and crack interaction.

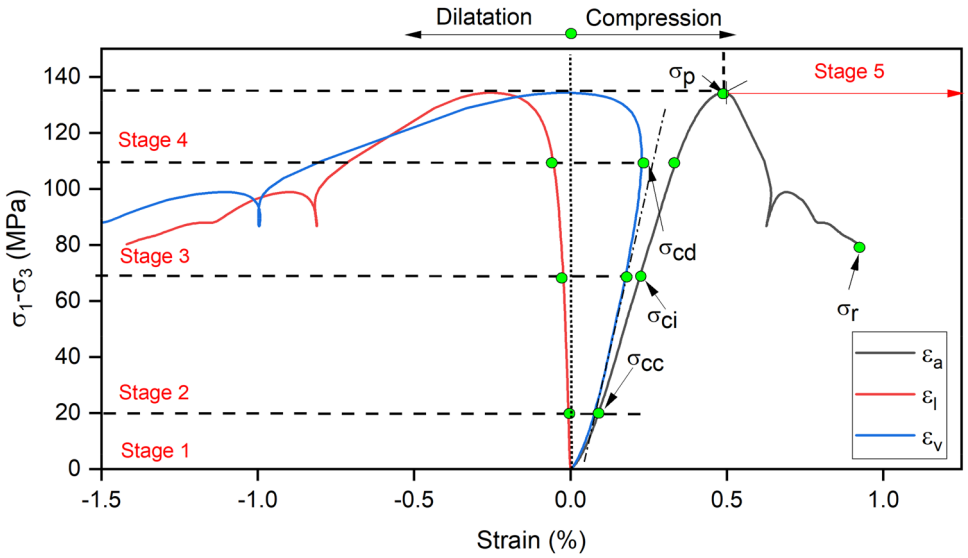

Fig. 1 Stress–strain relation and damage development stages of a limestone sample in a triaxial compression test (confining stress = 5 MPa). The plotted strains include volumetric strain (ε_v), axial strain (ε_a) and lateral strain (ε_l). The five damage development stages, i.e., compression stage, linear elastic stage, crack initiation and stable crack growth stage, crack damage and unstable crack growth stage and post-peak stage, are indicated and separated by the black dashed line. Stress thresholds (green dots) of these damage stages include crack closure (σ_{cc}), crack initiation (σ_{ci}), onset of dilatancy (σ_{cd}), peak strength (σ_p) and residual strength (σ_r)

The consensus among these strategies for fracturing damage division is that the inception of damage is marked by the threshold of crack initiation stress (σ_{ci}). σ_{ci} is a critical parameter not only for theoretical investigations of the mechanical behavior of rocks, but also for the stability analysis of engineering structures. First, it is the beginning of strength degradation and an important parameter for estimating the spalling stress level of the surrounding rock in an underground excavation face (Andersson and Martin 2009; Andersson et al. 2009; Martin and Christiansson 2009; Martin 1997). Second, it can be used to estimate the diameter of the excavation damage zone (EDZ) at the underground excavation boundary (Perras and Diederichs 2016). Third, it can be used to evaluate rock's brittleness (Wang et al. 2014; Xi et al. 2020). Fourth, it can be used as the lower-bound strength to estimate the long-term strength of engineering rock (Damjanac and Fairhurst 2010; Martin and Chandler 1994a). Last but not least, σ_{ci} is also important for strength criteria and constitutive models. More concretely, it can be used to estimate the parameter *mi* of the Hoek–Brown (H-B) criterion (Cai 2010), the uniaxial compressive strength (UCS) (Nicksiar and Martin 2013) and parameters in some constitutive models (Cieślik 2007; Palchik and Hatzor 2002; Peng et al. 2015; Wen et al. 2018).

During the past several decades, different methods have been proposed to determine σ_{ci} based on laboratory results, such as the volumetric strain method (VSM) (Brace et al. 1966), crack volumetric strain method (CVSM) (Martin and Chandler 1994a), instantaneous Poisson's ratio method (IPRM) (Diederichs 2007), lateral strain method (LSM) (Lajtai 1974), and lateral strain response method (LSRM) (Nicksiar and Martin 2012). These methods provide effective tools to identify σ_{ci} because the stress–strain relations are easily obtained by laboratory tests. However, these strain-based methods are subjective when plotting a tangent line of the linear portion of either the lateral strain, volumetric strain or Poisson's ratio curve. Therefore, results from these strain-based methods are inaccurate. Furthermore, the acoustic emission (AE) technique is a well-known tool and has been routinely applied in the fracturing investigation of engineering rocks (Li et al. 2017; Lockner 1995; Moradian et al. 2016; Xu et al. 2017; Zhang et al. 2015; Zhao et al. 2013a; Zhou et al. 2019). Apart from the AE technique, other approaches have also been adopted to identify σ_{ci}, e.g., high-speed photography (Rousseau and Tippur 2001, 2002), electrical resistivity (Samouëlian et al. 2004), laser speckle interferometry (Mohr and Henn 2007; Steinzig and Ponslet 2003) and numerical modeling (Fan et al. 2018; Li et al. 2018a), etc. However, these techniques are more resource-intensive and time-consuming than those strain-based approaches.

This paper aims to propose a new volumetric strain-based method, i.e., the volumetric strain response method (VSRM), to determine σ_{ci}. The VSRM is based on two novel concepts, i.e., i.e., the dilatancy resistance state index (δ_{ci}) and the maximum value of the dilatancy resistance state index difference ($|\Delta\delta_{ci}|$). The practicability of the proposed VSRM is examined by experimental results, and then compared with other methods. Furthermore, engineering rocks are usually exposed to water, containing chemical ions and showing acidity (Brantley et al. 2008; Williams 2008). The chemical dissolution leads to strength degradation and failure acceleration of rocks (Jeffery and Hutchison 1981; Li et al. 2018c). Research on mechanical responses of the chemically corroded rocks is important for many engineering constructions, e.g., tunnels (Chapman et al. 2017), nuclear waste storage (Ben Abdelghani et al. 2015; Tsang et al. 2000) and geologic carbon sequestration (GCS) (Grgic 2011; Rutqvist and Tsang 2002; Zhang et al. 2016), etc. In this study, we extend the application of the proposed VSRM to investigate the influences from chemical corrosion, quantified and characterized using nuclear magnetic resonance (NMR) technology, as well as the impact of confining stress on both σ_{ci} and $\Delta\delta_{ci}$ of the carbonate rocks.

2 Standard Methods to Identify the Crack Imitation Stress Threshold (σ_{ci}) of Rocks Under Compression

Some strain-based methods have been proposed to identify the crack imitation stress threshold (σ_{ci}). The most common feature of these methods involves the strains measured in laboratory tests, i.e., either the axial strain, lateral strain, volumetric strain or crack volumetric strain. In the past several decades, new techniques, such as the acoustic emission (AE) technique, are adopted to measure σ_{ci}. These methods are briefly reviewed below.

2.1 Volumetric Strain Method (VSM)

Brace et al. (1966) and Bieniawski (1967b) investigated the stress–strain relation of marble, granite, quartzite, aplite and norite. They suggested that the σ_{ci} could be identified using volumetric strain by examining the point at which the volumetric strain deviated from its linear region (see Fig. 2). The volumetric strain is calculated as follows (Brandtzaeg et al. 1928; Cook 1970):

$$\varepsilon_v = \frac{\Delta V}{V} = \varepsilon_a + 2\varepsilon_l \tag{1}$$

where ΔV is the volume change and V is the original volume, ε_v is the volumetric strain, ε_a is the axial strain, ε_l is the lateral strain.

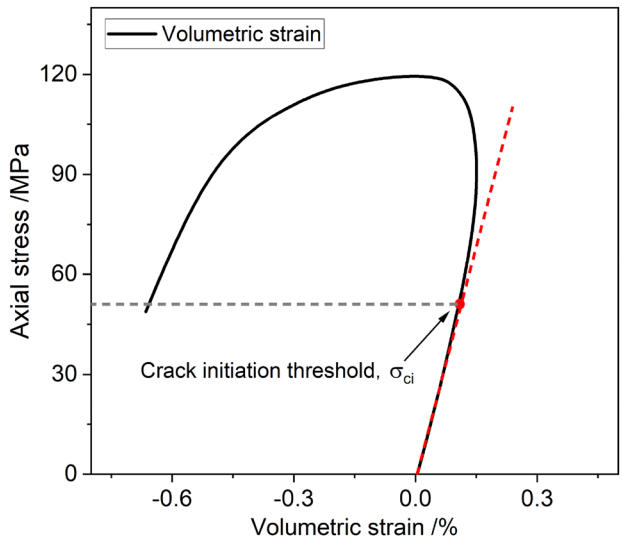

Fig. 2 Volumetric strain method (VSM) proposed by Brace et al. (1966)

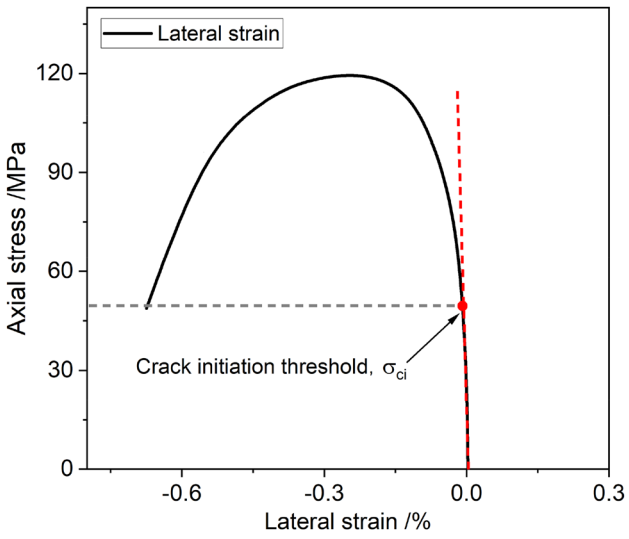

Fig. 3 Lateral strain method (LSM) proposed by Lajtai (1974)

The VSM is practical because of its simplicity and high efficiency. However, the VSM is subjective. It is based on the user's judgment to plot a tangent line along the approximately linear section of the volumetric strain curve. The endpoint of the linear region of the volumetric strain curve (i.e., σ_{ci}) depends on the user's intuition. Therefore, the accuracy of the VSM cannot be guaranteed. And errors are easily yielded when identifying σ_{ci}, the point at which the volumetric strain curve begins to deviate from its linear part.

2.2 Lateral Strain Method (LSM)

Lajtai (1974) first proposed a lateral strain-based method to determine σ_{ci} based on the lateral strain. In this method, σ_{ci} corresponds to the endpoint of the linear region of the lateral strain (see Fig. 3). The LSM has similar advantages to the VSM, such as being simple, easy to use and intuitive. Nevertheless, the LSM is also subjective and depends on the user's judgment for the endpoint of the linear portion. Therefore, inaccuracy is easily yielded using the LSM, especially when the rock sample contains intense pre-existing cracks. Eberhardt et al. (1998) investigated the lateral stiffness (i.e., the ratio of axial stress to lateral strain) evolution of gray and pink granite under compression. They found that the linear part of the lateral stiffness curve never occurred. Instead, the lateral stiffness continuously decreased during the whole loading process (i.e., from beginning to failure), indicating that the axial stress-lateral strain curve is not genuinely linear at both pre- and post-peak regions. In this case, the LSM may yield inaccurate results.

To overcome the subjectivity of the LSM, Nicksiar and Martin (2012) proposed a lateral strain response method (LSRM) to measure σ_{ci}. The LSRM is more objective than the LSM, and provides a simple mathematical equation to process large amount of discrete data points. However, the physical meaning of the parameters and theoretical background of the LSRM are ambiguous and not explained. For example, the reason for the axial stress corresponding to the maximum lateral strain difference is σ_{ci} is very unclear and not theoretically discussed.

2.3 Instantaneous Poisson's Ratio Method (IPRM)

Diederichs (2007) proposed the instantaneous Poisson's ratio method (IPRM) to identify the σ_{ci}. Using the plot of the instantaneous Poisson's ratio versus the axial stress, σ_{ci} can be identified by the onset point where the curve deviated from the linear region (see Fig. 4). However, the LSM and the VSM cannot accurately identify the σ_{ci}, neither does the IPRM.

2.4 Axial Stiffness Method (ASM)

Gao et al. (2018a) proposed the axial stiffness method (ASM) to determine the σ_{ci}. This method is based on the plot of the axial stiffness (i.e., the ratio of axial stress to lateral strain) versus axial strain. Similar to the LSM, VSM and IPRM, the σ_{ci} corresponds to the onset point where the curve deviates from the horizontal region. The LSM, VSM and IPRM cannot accurately identify the σ_{ci}, neither does the ASM. Furthermore, another disadvantage of the LSM, LSRM and ASM is that they only consider one of the two strains (i.e., either the axial or lateral strain) and ignore the other. Rock is a heterogeneous geomaterial, consisting of cement and mineral grains, where pores and cracks are scattered. The stress-induced crack may

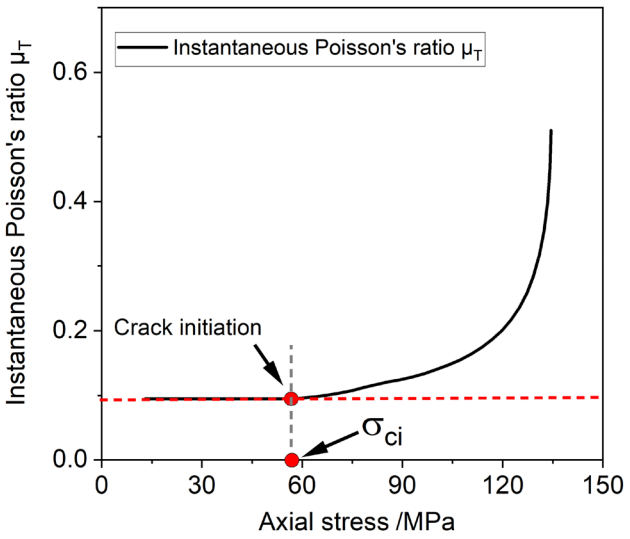

Fig. 4 Instantaneous Poisson's ratio method proposed by Diederichs (2007)

lead to heterogeneous deformation on both sides (lateral and axial). The volumetric strain considers both the influences of the lateral and axial strains, which makes it a more comprehensive and credible parameter for identifying the crack initiation threshold. On this basis, to overcome the objectivity and utilize the advantages of the volumetric strain, the crack volumetric strain method (CVSM) is proposed and presented in the following sections.

2.5 Crack Volumetric Strain Method (CVSM)

Martin and Chandler (1994a) proposed the crack volumetric strain method (CVSM) based on the volumetric strain. In CVSM, σ_{ci} is identified by a plot of crack volumetric strain versus axial strain. And σ_{ci} corresponds to the onset point where the curve deviated from the horizontal region (see Fig. 5). The crack volumetric strain is defined with the following equations:

$$\varepsilon_{ve} = \frac{\Delta V}{V_{elastic}} = \frac{1-2\mu}{E}(\sigma_1 + 2\sigma_3) \tag{2}$$

$$\varepsilon_{vc} = \varepsilon_v - \varepsilon_{ve} \tag{3}$$

where ε_{ve} is the elastic volumetric strain, ε_{vc} is the crack volumetric strain, E and μ are Young's modulus and Poisson's ratio, respectively. Note that E and μ are the elastic constants of the rock, belonging to the damage stage 2 (elastic stage).

The CVSM is objective. However, one drawback of the CVSM is that the elastic parameters (i.e., E and μ), especially μ, may introduce uncertainty and inaccuracy in the determination of σ_{ci}. What's more, μ cannot be accurately calculated when there are a large number of pre-existing cracks in rocks (Eberhardt et al. 1998). There is no linear

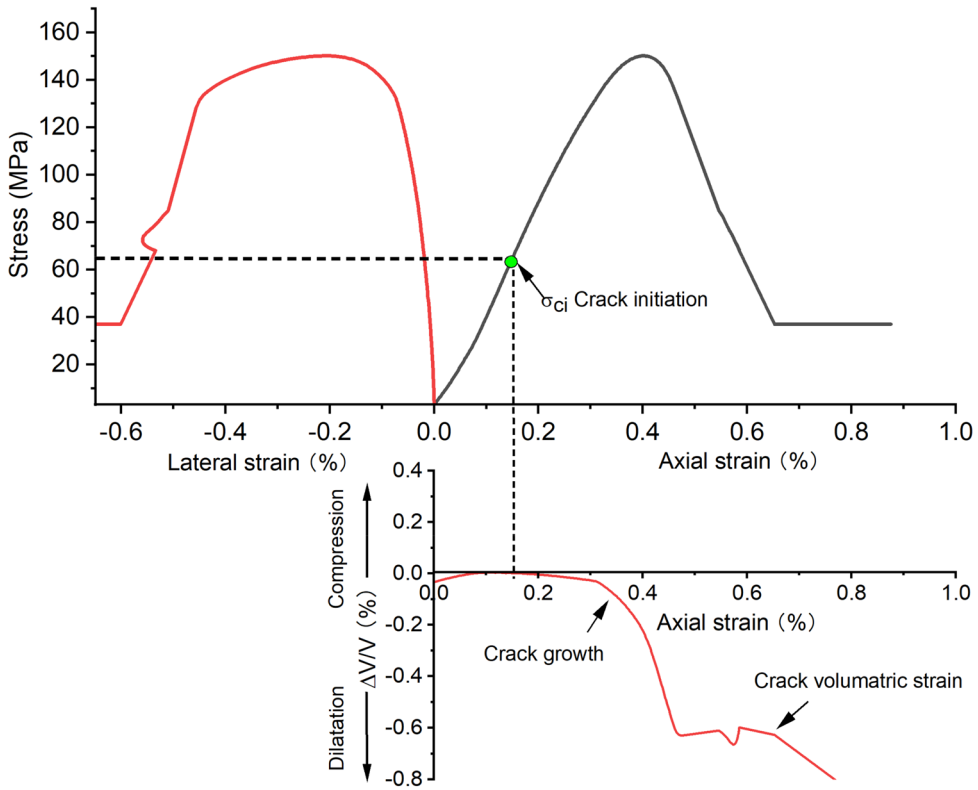

Fig. 5 Crack volumetric strain method (CVSM) proposed by Martin and Chandler (1994a)

region in the lateral strain curve of such highly cracked rock. As a result, μ is approximately calculated by the ratio of lateral to axial strain magnitudes of the best approximate straight region of lateral strain. This method not only increases complicity in the determination of μ but also introduces inaccuracy and uncertainty in the determination of the σ_{ci}. For instance, a change in the Poisson's ratio of $\pm$ 0.05 may lead to a change in σ_{ci} of $\pm$ 40% (Eberhardt et al. 1998).

2.6 Acoustic Emission (AE) Method

Acoustic emission (AE) is a low-energy seismic event caused by damage development, e.g., grain crashing or crack initiation. AE technology has been employed to investigate large scale excavations when damage occurs at the excavation boundary (Cai et al. 2007; Smith et al. 2014). As shown in Fig. 6, AE technology also has been adapted to damage investigation of rock samples at a laboratory scale (Chang and Lee 2004; Zhang et al. 2023; Zhao et al. 2013a). The AE method has two major problems: the first is to choose a proper threshold for the AE signals, which is adequately high to purify the background noise and low to identify the micro-crack initiation (Singh 2016; Xue et al. 2014). Second, the uniqueness and the accuracy of the endpoint of the linear region of the cumulative AE hit curve cannot be guaranteed (Gao et al. 2018b).

In summary, stress and strain are the most commonly available data for a rock sample in laboratory tests, as they can be easily and directly measured by the stress and strain gauges. The strain-based method becomes the most effortless, efficient and economical approach for determining the damage thresholds of the laboratory-scale rock samples. Furthermore, the thresholds, e.g., the dilatancy boundary, peak and residual strength, can be directly and objectively determined from the stress–strain curve. Therefore, the strain-based method has been widely accepted and recognized by many researchers, e.g., (Gao et al. 2018b; Gao et al. 2020; Nicksiar and Martin 2012, 2013; Palchik 2010; Ranjith et al. 2010; Xue et al. 2014). In the following sections, we will propose a new strain-based method to determine σ_{ci}. This method is based on the volumetric strain and reduces subjectivity.

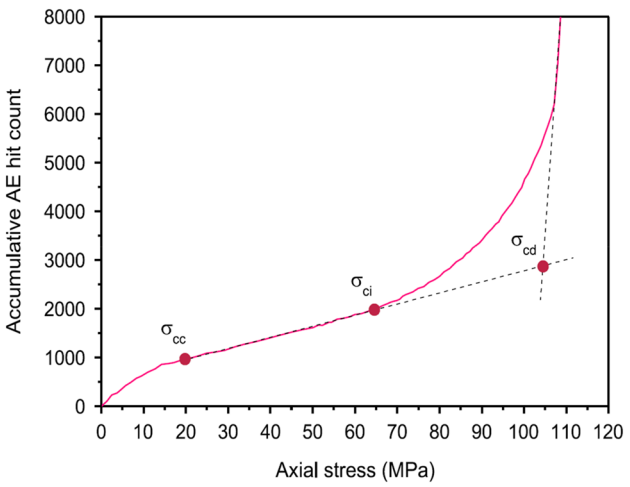

Fig. 6 Relationship between AE hit count and axial stress for identifying the σ_{ci}. The data are sourced from the test conducted by Zhao et al. (2013a) as shown in their Fig. 4. σ_{ci} is the ending point of the linear region of the cumulative AE hit curve

3 Experimental Tests on Jinyun Limestone

To propose a new method for identifying σ_{ci}, stress–strain curves, strength and deformation responses, damage initiation characteristics and mechanisms should be experimentally investigated first. This section details the experimental methodology. The VSRM will be proposed based on this laboratory investigation and presented in the next section.

3.1 Experimental Setup and Procedure

3.1.1 Sample Preparation

Limestone, a common carbonate rock in the karst area for many engineering applications, was selected as the test sample. We collected the limestone samples from Jinyun Mountain. Jinyun Mountain is dominated by sedimentary rocks (e.g., limestone and sandstone) and located in the karst mountain area in Sichuan Basin. The samples were drilled from the rock blocks without macroscopic cracks and polished into a smooth-ended cylindrical shape with a length of 100 mm and a diameter of 50 mm (see Fig. 7b). According to the rock mineral composition analysis, the limestone consists of 59% calcite, 22% dolomite, 12% feldspar and 7% cement and accessory minerals, such as pyrite, limonite, quartz, and bioclastic.

The water sample was also collected from Jinyun Mountain. Using the ion chromatography method, the result showed that the main ions in the water were Na^+, Ca^{2+}, Mg^{2+}, SO_4^{2-}, Cl^- and HCO_3^-. The pH value of the water sample is 6. Among these six ions, Na^+ and SO_4^{2-} account for the highest proportion. It is efficient to simulate the chemical effect on the rock in a simplified system. (Brantley et al. 2008). To avoid the "Homoionic effect" with calcite and dolomite, the Na_2SO_4 solution was chosen. Hem (1959) reported that the pH of natural water ranges from 1.9 to 9.4. In this study, three pH values (3, 5 and 7) of the Na_2SO_4 solution were used. Their initial concentrations were 0.01 mol L^{-1}.

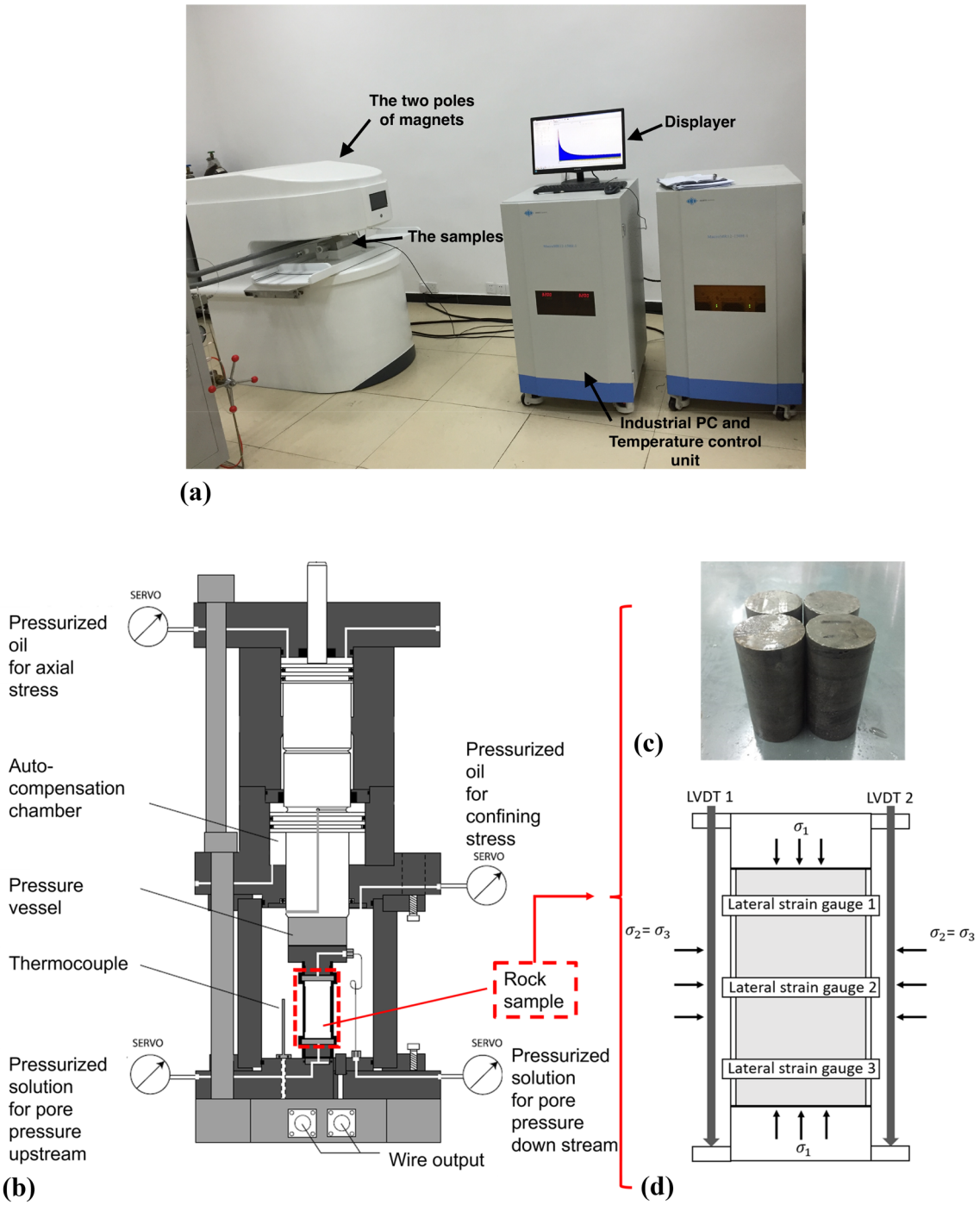

Fig. 7 Rock testing facility: **a** NMR system. **b** Schematic of the triaxial cell. **c** Photo of the limestone samples. **d** Schematic of the sample cell

3.1.2 Experimental Facility

The nuclear magnetic resonance (NMR) system was applied to quantify and characterize the chemical corrosion effects (see Fig. 7a). The NMR system measures the signal intensity of hydrogen atoms in the fully water saturated rock and outputs transverse relaxation time distribution (T_2 spectrum), porosity and magnetic resonance imaging (MRI). Uniaxial and triaxial compression tests were conducted using a triaxial cell. Figure 7a shows the schematic of the triaxial cell, which is controlled by three pressurized oil pumps. The

axial stress and confining stress are provided by the first and second oil pumps, respectively. The third oil pump is for pore pressure control, which is not used in this study. The real-time measured data are recorded by the data acquisition system. Figure 7c shows the magnified view of the sample section, and the gray shaded area represents the rock sample. The sample is isolated using polyolefin membranes (2 mm in thickness) and then put in the testing cell. The axial strain is measured by two linear variable differential transformers (LVDT) and the lateral strain is measured by three strain gauges.

3.1.3 Testing Procedure

It should be noted that the carbonate dissolution in karst areas is a long-term chemical reaction (decades or even centuries). When the karst rock is subject to short-term mechanical damages (i.e., the excavation of underground constructions), carbonate dissolution (i.e., chemical damage) in this period is regarded as negligible. Therefore, the term ''C-M" in this study is unidirectional and referred to as a sequentially coupled C-M condition.

The testing procedure was designed as follows:

1. The samples were saturated with a vacuum saturation machine for 24 h. After that, their porosity was determined by the NMR. Samples with equal initial porosity and mass were chosen in this test.
2. The samples were categorized into five groups and immersed in distilled water or Na_2SO_4 solutions for 60 days. Table 1 shows the testing matrix with different confining stress, corrosion time and pH value of the solution. After reaching the final corrosion period (i.e., 60 days), the porosity of the samples was measured. After that, the ion concentration of the solution was measured using the ion chromatography method.
3. The samples were put into the triaxial cell for testing. Limestone samples were deformed with a constant confining pressure ($\sigma_2 = \sigma_3$) of 0 MPa (uniaxial compression tests), 5 MPa, 10 MPa, 20 MPa, 30 MPa, respectively. Initially, σ_1, σ_2 and σ_3 were applied with pre-set hydrostatic pressures (5 MPa, 10 MPa, 20 MPa, 30 MPa, respectively) with a loading rate of 0.2 MPa/s. Then the confining pressures ($\sigma_2 = \sigma_3$) was fixed and the axial stress (σ_1) was increased at a rate of 0.02 mm min^{-1} until the sample was ruptured. After that, the sample is removed from the triaxial cell.
4. After the above uniaxial and triaxial compression tests, the stress–strain curves could be obtained. The damage stages and their damage thresholds (i.e., σ_{cc}, σ_{ci}, σ_{cd}, σ_p and σ_r) could also be characterized. To better reveal failure mechanisms and show details of microcrack development in samples, a combination of arrested compression tests and scanning electron microscopy (SEM) tests were conducted. The testing procedure was as follows. Samples were divided into five groups (E-I) with two samples in each group (see Table 2). These samples were loaded to the threshold of damages stably development stage (σ_{ci}) and damage accelerate stage (σ_{cd}), which were determined from the stress–strain curves obtained from the previous step. After the damage threshold was reached, these partially loaded samples were then carefully removed from the triaxial cell. Then

Table 1 Testing matrix with the confining stress, pH value of the solution and corrosion durations

No. of specimen	Confining stress/MPa	pH value	Corrosion time/days	No. of specimen	Confining stress/MPa	pH value	Corrosion time/days
A-1	0	3	60	C-1	0	7	60
A-2	5			C-2	5		
A-3	10			C-3	10		
A-4	20			C-4	20		
A-5	30			C-5	30		
B-1	0	5	60	D-1	0	Distilled water	60
B-2	5			D-2	5		
B-3	10			D-3	10		
B-4	20			D-4	20		
B-5	30			D-5	30		
E-1	0	Dry sample	–				
E -2	5						
E -3	10						
E -4	20						
E -5	30						

Table 2 List of the partially loaded dry samples in arrested compression tests

No. of specimen	Confining stress/MPa	Loading state	No. of specimen	Confining stress/MPa	Loading state
F-1	0	Loaded to σ_{ci}	I-1	20	Loaded to σ_{ci}
F-2	0	Loaded to σ_{cd}	I-2	20	Loaded to σ_{cd}
G-1	5	Loaded to σ_{ci}	J-1	30	Loaded to σ_{ci}
G-2	5	Loaded to σ_{cd}	J-2	30	Loaded to σ_{cd}
H-1	10	Loaded to σ_{ci}			
H-2	10	Loaded to σ_{cd}			

σ_{ci} and σ_{cd} denote the threshold of damages stably development stage and damage accelerate stage, respectively. In this arrest compression test, σ_{ci} is 45% peak strength and σ_{cd} is 85% peak strength

SEM was used to view the microstructural changes. For SEM examination, a 1 cm^3 core was taken from the partially loaded sample. Then an approximately 200 Å thick layer of gold–palladium was applied on the surface of the cube. After that, this cube will be put in an SEM system for analysis.

3.2 Stress–Strain Curves and Dilatancy Boundary

Figure 8 shows the stress–strain curves of the limestone samples in uniaxial and conventional triaxial compression tests. Axial strain (ε_{axial}), lateral strain ($\varepsilon_{lateral}$) and volumetric strain (ε_v) of the limestone samples, corroded by pH 3, pH 5, pH 7 Na_2SO_4 solution and distilled water for 60 days, deformed at confining stresses of 0 MPa, 5 MPa, 10 MPa, 20 MPa and 30 MPa, are presented in Fig. 8.

Several important characteristics are observed from the stress–strain relations:

1. Chemical effects and confining stress significantly influence rock's compressive strength (i.e., the peak and residual strength), strain (i.e., the axial, lateral and volumetric strain) and failure characteristics. Under the same chemical corrosion conditions (i.e., same pH value of the solution and corrosion periods), both the peak and residual strength increase with the increase of confining stress. Under the same confinement, the samples softened by distilled water always have higher peak and residual strength than those corroded by acid chemical solution, and the samples immersed in pH 3 solution have the lowest strength. Additionally, it should be noted that, coupled with chemical effects, confinement's contribution to the bearing capacity (i.e., the peak strength of rock) growth is restrained. More concretely, for samples corroded by pH 3 solution for 60 days, when the confinement is 5 MPa, 10 MPa, 20 MPa and 30 MPa, rock's peak strength shows an increase of 45.93%, 73.28%, 103.24% and 135.48% compared with the uniaxial compressive strength (UCS). While for those softened by distilled water, under the same confinements, rock's peak strength shows an increase of 52.79%, 81.24%, 131.20% and 161.71% compared with the uniaxial compressive strength (UCS). In summary, the chemically corroded limestone is more prone to breaking, showing lower bearing capability.
2. The reverse point in the volumetric strain curve marks the beginning of dilatancy, regarded as the dilatancy boundary σ_{cd}. Figure 9 shows the volumetric strain (ε_v^{cd}) and deviatoric stress (σ_{cd}) at the dilatancy threshold of the limestone samples. From Fig. 9, we can find that the beginning of dilatancy is delayed with confinement growth, and chemical corrosion effects accelerate dilatancy starts. More concretely, under the same pH condition, ε_v^{cd} and σ_{cd} increase with confinement growth. Under the same confinement, the samples softened by distilled water always have higher ε_v^{cd} and σ_{cd} than those corroded by acid chemical solution, and the samples immersed in pH 3 solution have the lowest ones.

4 The Volumetric Strain Response Method (VSRM)

4.1 Derivation of the VSRM

As suggested by Brace and Bieniawski (Bieniawski 1967a, 1968, 1967b; Brace et al. 1966), the volumetric strain is an effective index of rock stress-induced damage evolution. Therefore, the proposed method is based on the volumetric strain. As shown in Fig. 10a, the dilatancy boundary σ_{cd} (i.e., the turning point of the volumetric strain curve) marks the endpoint of the compressive stage and the beginning of dilatancy. The volumetric strain shows compressive deformation before the σ_{cd} and dilatancy deformation after the σ_{cd}. The mechanical response of rock before the dilatancy boundary σ_{cd} reflects a dilatancy-resist process. As the dilatancy boundary approaches, the rock's corresponding dilatancy-resist capability gradually decreases. Crack damage development is the root cause of dilatancy resistance degradation. And the crack initiation threshold σ_{ci} marks the beginning of the degradation of dilatancy resistance (this will be discussed in detail in the next section, i.e., Sect. 4.2). Therefore, the volumetric strain

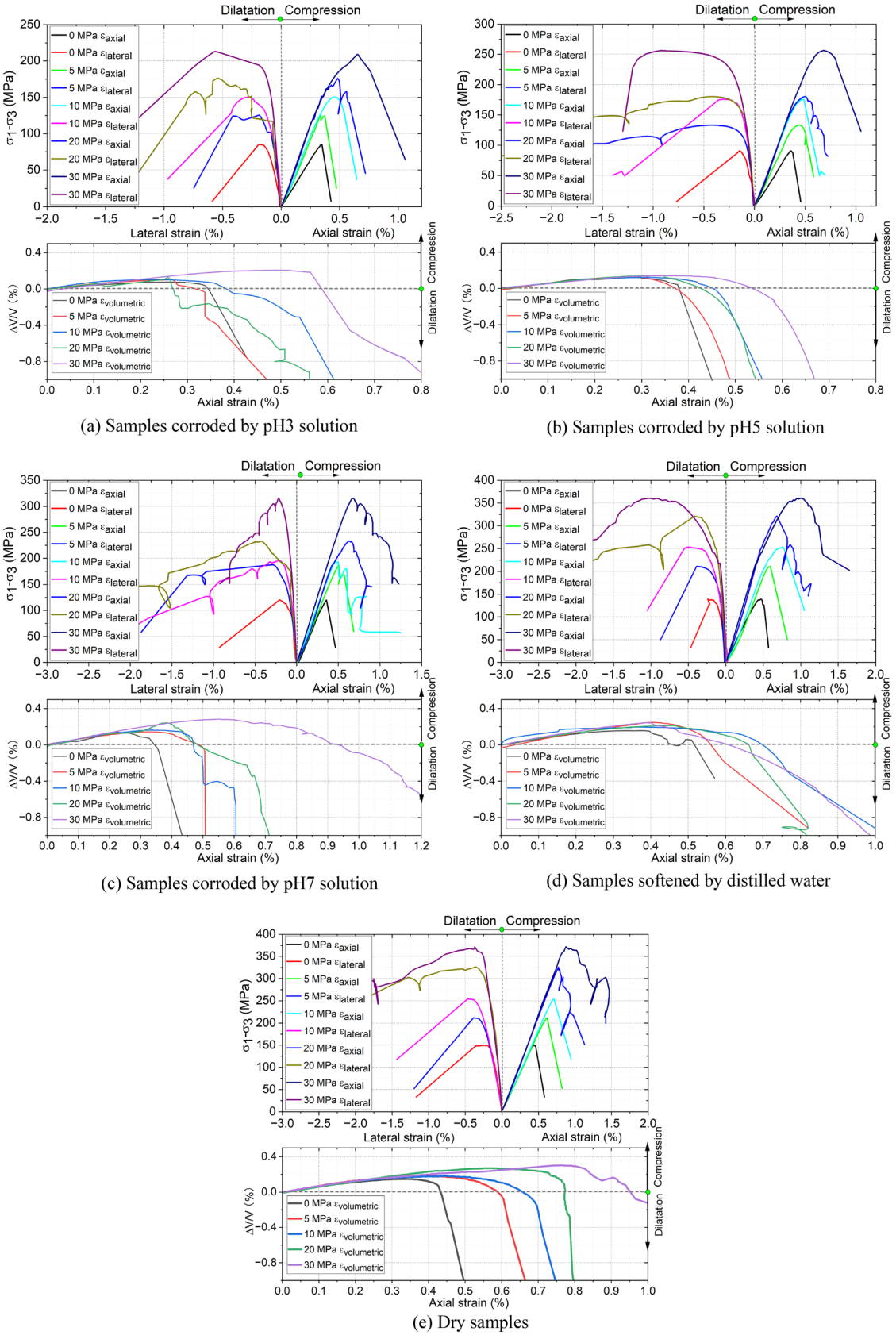

(a) Samples corroded by pH3 solution

(b) Samples corroded by pH5 solution

(c) Samples corroded by pH7 solution

(d) Samples softened by distilled water

(e) Dry samples

Fig. 8 Stress–strain diagram of the chemically corroded limestone samples in uniaxial and triaxial compression tests

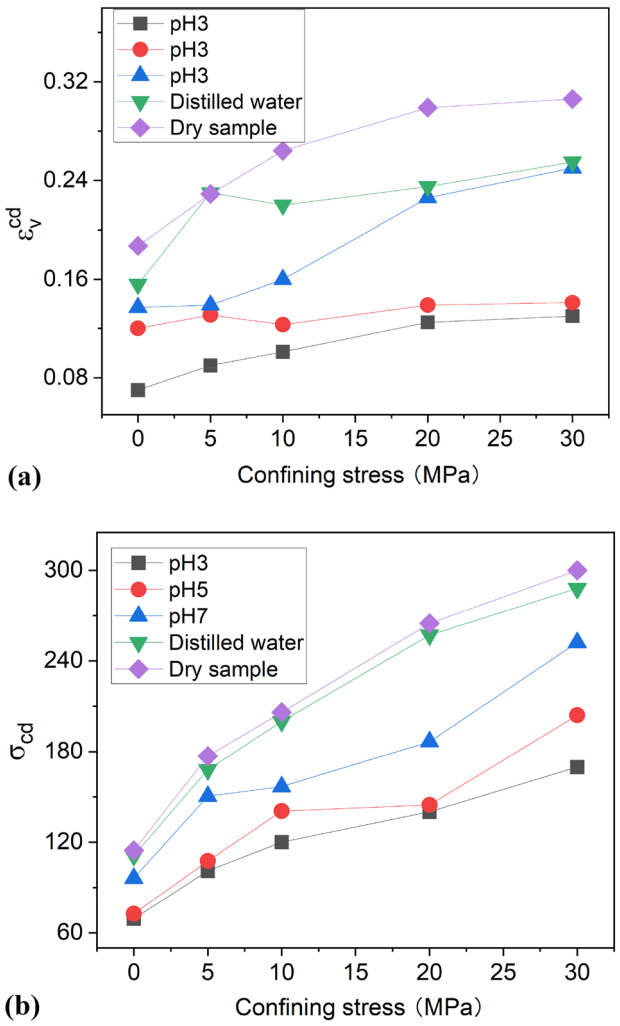

Fig. 9 Variation of the volumetric strain (ε_v^{cd}) and deviatoric stress (σ_{cd}) at the dilatancy threshold. **a** ε_v^{cd} versus confining stress. **b** σ_{cd} versus confining stress

curve departs its linear part, deflects concave upward and becomes steeper and steeper with a diminishing dilatancy resistance after σ_{ci}, showing a decreasing compression deformation rate. The compression deformation rate decreases to zero at the dilatancy boundary σ_{cd}. The volumetric strain becomes the dilatancy strain after σ_{cd} with an increasing dilatancy deformation rate until the final failure. In this case, if we draw a reference line connecting zero stress and σ_{cd} (see the solid red line in Fig. 10a), the stress corresponding to the peak point of the "U shape" volumetric strain curve belongs to σ_{ci}. The VSRM can be proposed now based on the mechanisms described above.

To show the dilatancy resistance and compression states of the rock, a new dilatancy resistance state index, δ_{ci}, is proposed and given in Eq. (4).

$$\delta_{ci} = 1 - \frac{\varepsilon_v}{\varepsilon_v^{cd}} \tag{4}$$

where ε_v is the volumetric strain and ε_v^{cd} is the volumetric strain at the dilatancy boundary. δ_{ci} reflect the state of dilatancy resistance of the rock during the compressive period, ranging from 1 to 0. When the rock is not deformed (i.e., $\varepsilon_v = 0$), the δ_{ci} is 1. When the volumetric strain reaches the dilatancy threshold (i.e., ε_v^{cd}), the δ_{ci} decreases to zero. The decrease of the δ_{ci} from 1 to 0 indicates that the rock is undergoing the compressive process from the initial condition (i.e., $\sigma_1 = 0$ and $\varepsilon_v = 0$) to the beginning of dilatancy (i.e., $\sigma_1 = \sigma_{cd}$ and $\varepsilon_v = \varepsilon_v^{cd}$). Meanwhile, its dilatancy resistance and compressibility is decreasing and the dilatancy behavior is approaching. To better study the compressive state during the compressive stage and easier compare the compressive states of the rocks under different loading condition, the volumetric strain is normalized by the dilatancy resistance state index δ_{ci}. From a mathematical perspective, the volumetric strain is normalized by Eq. 4, and its shape and deflection point (peak point) remain.

With the help of δ_{ci}, the VSRM is then proposed. Data of sample E-1 is chosen as an example and shown in Fig. 10 to illustrate the derivation process of the VSRM. The detailed methodology is as follows:

1. Determine the stress and strain (i.e., σ_{cd} and ε_v^{cd}) at the dilatancy boundary (see Fig. 10a). Then calculate the dilatancy resistance state index δ_{ci} using Eq. (4).
2. Plot the diagram of deviatoric stress ($\sigma_1 - \sigma_3$) versus δ_{ci}. Then draw a linear reference line that connects σ_{cd} and zero stress (see Fig. 10b).
3. Calculate the difference value (i.e., the dilatancy resistance state index difference, $\Delta\delta_{ci}$) between the δ_{ci} and the linear reference line.
4. Plot the diagram of the deviatoric stress ($\sigma_1 - \sigma_3$) versus the absolute dilatancy resistance state index difference ($|\Delta\delta_{ci}|$). The σ_{ci} corresponds to the maximum of $|\Delta\delta_{ci}|$ (see Fig. 10c).

4.2 Physical Meaning of the Dilatancy Resistance Index Difference ($\Delta\delta_{ci}$)

The mechanisms of the proposed VSRM have been presented in Sect. 4.1. To provide a more comprehensive understanding of the VSRM and explain the significance of the maximum $|\Delta\delta_{ci}|$ associated with the σ_{ci}, it is necessary to delve into the damage mechanism of rocks under compression, elucidating its physical interpretation. To visualize the damage development at each stage and further investigate the failure mechanisms, SEM tests were conducted at a microscopic scale of 2–200 μm. Figure 11 shows the SEM

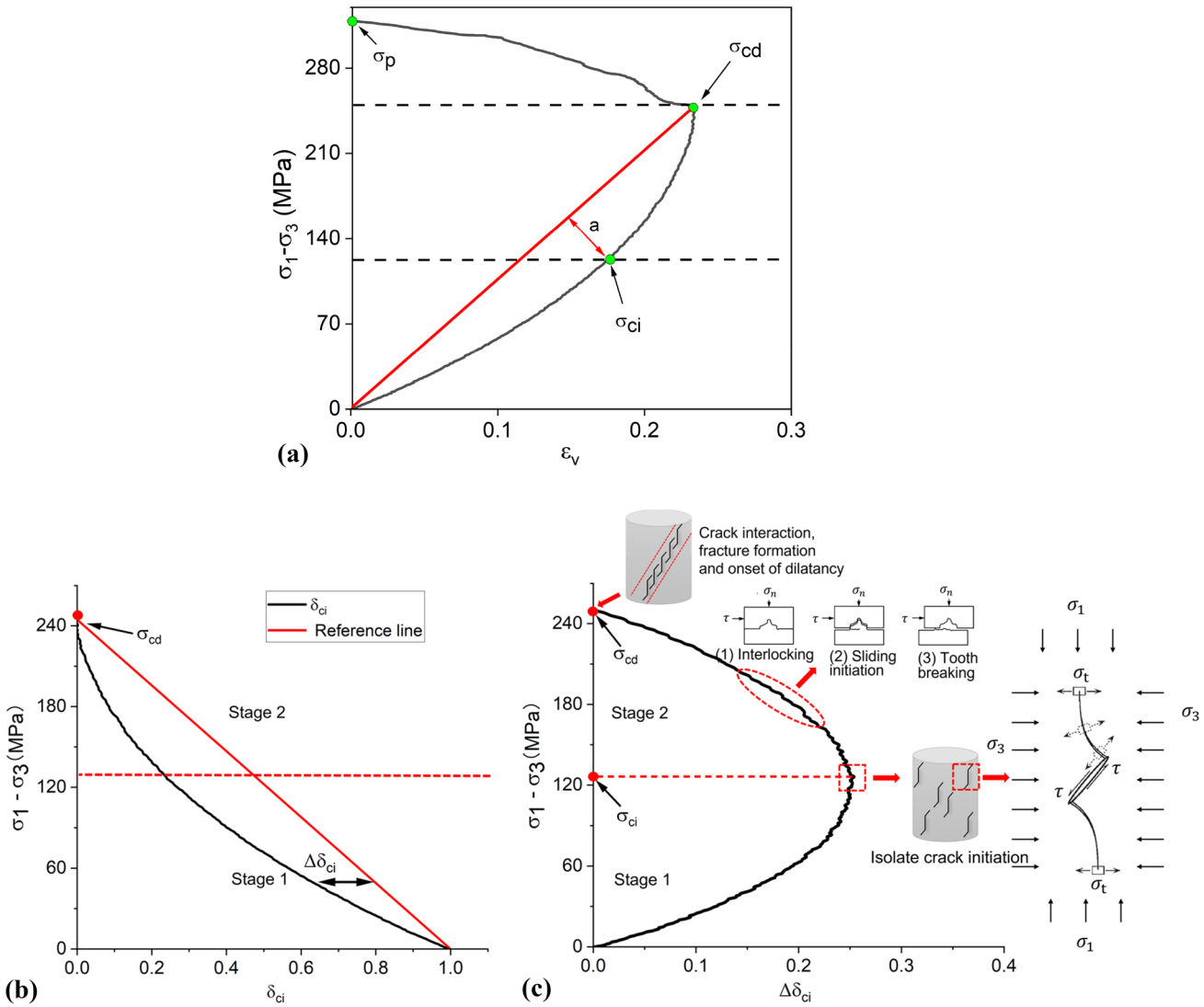

Fig. 10 Schematic of the determination of the crack initiation threshold utilizing the proposed volumetric strain response method (VSRM). **a** Deviatoric stress ($\sigma_1 - \sigma_3$) versus volumetric strain (ε_v). Stress thresholds (green dots) of these damage stages include crack initiation (σ_{ci}), onset of dilatancy (σ_{cd}) and peak strength (σ_p). **b** Deviatoric stress ($\sigma_1 - \sigma_3$) versus dilatancy resistance state index (δ_{ci}). **c** Deviatoric stress ($\sigma_1 - \sigma_3$) versus dilatancy resistance index difference ($\Delta\delta_{ci}$). Stage 1: interlocking stage; Stage 2: shear sliding stage

image at thresholds of the crack initiation and dilatancy. The recognition of new stress-induced cracks is based on the following criteria: most stress-induced micro-cracks are long and narrow with sharp ends, while the natural pores are blunt, bridged and discontinuous.

There are two types of natural pores observed in the sample: scattered small circular pores (Fig. 11b) and crack-like pores (Fig. 11c). Thus, limestone can be treated as a dual-porosity medium. We also find that crack development (i.e., crack initiation, interaction and coalescence) is mainly dominated by crack-like pores, while the small circular pores are almost intact during the whole loading process. This is different from the prediction of theoretical models, e.g., Sammis and Ashby (1986), which assume that the crack initiation possibility of either the large or small pores is the same.

The damage development of the rock during the compression phase can be described as follows: initially, when a limestone sample undergoes uniaxial or triaxial compression, crack closure occurs (damage stage 1), leading to a concave region on the stress-volumetric strain curve (refer to Fig. 11a). Subsequently, as the cracks interlock due to roughness of their surfaces, the sample enters the elastic stage. The frictional resistance increases with the applied load, restraining the movement between crack surfaces. Although no new cracks initiate during this stage,

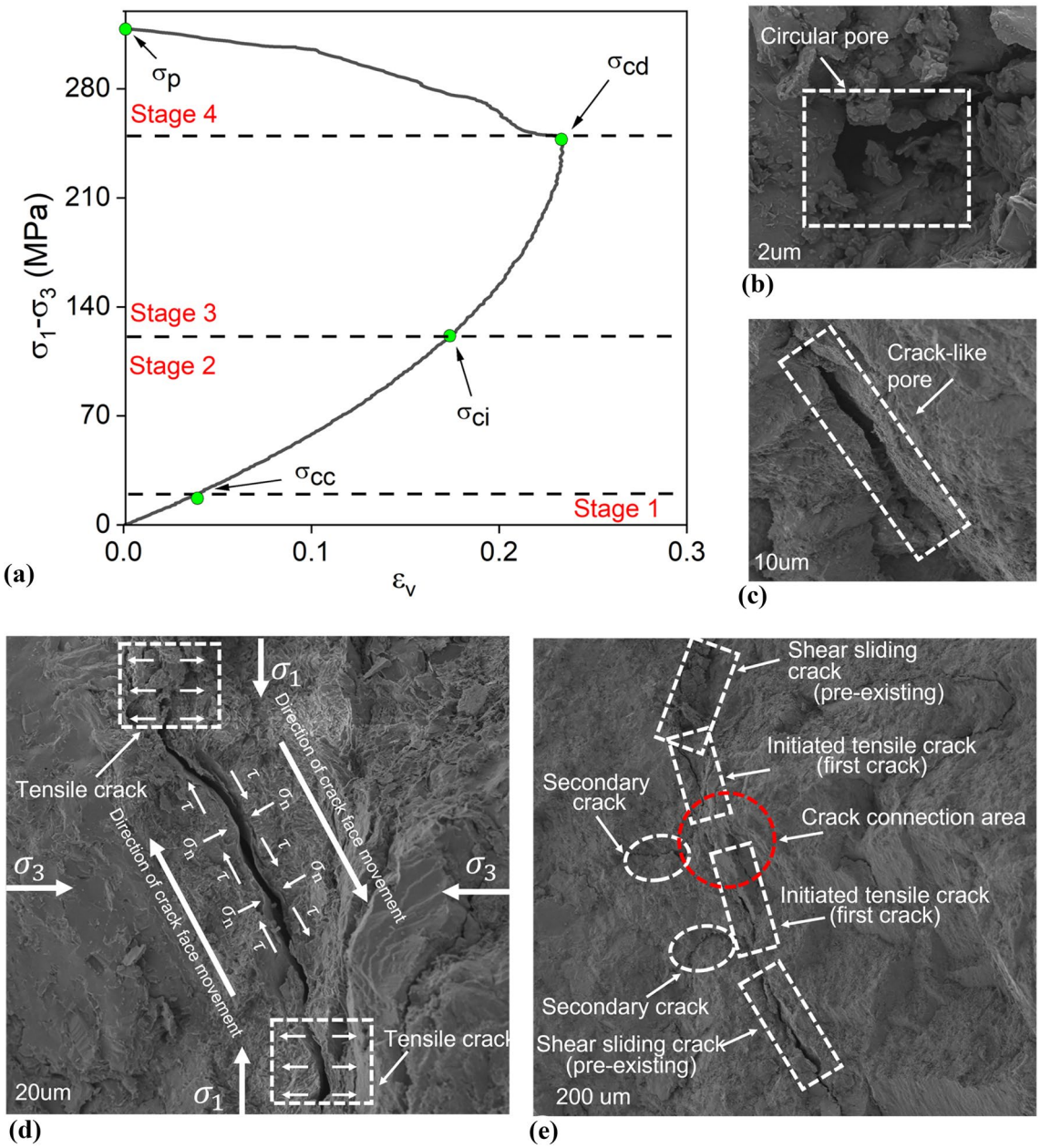

Fig. 11 Microscopic to macroscopic damage development mechanisms of the limestone sample under compression. **a** Deviatoric stress versus volumetric strain, showing the stress damage thresholds and the corresponding damage stages. **b** A typical circular pore. **c** A typical crack-like pore. **d** SEM image of the first cracks initiation at σ_{ci}. A micro shear zone is developed and the movement of the crack surface is marked with white arrows. Short tensile microcrack emanates from each tip after sliding between the faces of crack-like pores. **e** SEM image of crack connection at the dilatancy boundary σ_{cd}, showing the mechanism of dilatancy

the sample continues to undergo compaction through the adjustment of mineral grain position and elastic deformation of the skeleton. Consequently, the rock experiences continuous compaction prior to reaching the crack initiation stress threshold (σ_{ci}), resulting in a steady growth of the volumetric strain.

When the axial stress reaches σ_{ci}, the frictional shear resistance resulting from the interlocking of crack surfaces is surpassed, leading to shear sliding movement between the faces of individual cracks. This shear sliding generates micro shear zones, as depicted in Fig. 11d, and triggers the stable initiation of tensile cracks from the tips of crack-like pores. This phenomenon of sliding-induced tensile crack (first

crack) has been observed not only in rocks but also in other materials, such as glass (Brace and Bombolakis 1963; Hoek and Bieniawski 1965), ice (Schulson et al. 1991), plaster (Lajtai 1971) and hard plastics (Cannon et al. 1990; Nemat-Nasser and Horii 1982). The newly initiated tensile cracks propagate along the axial stress direction, causing lateral expansion. As a result, the lateral strain begins to grow at a faster rate than the axial strain, leading to the appearance of a deflection point (i.e., σ_{ci}) on the volumetric strain curve.

With further increase in the applied load, more shear sliding movement occur, leading to a significant increase in the number and size of tensile cracks. This, in turn, causes a gradual increase in the growth rate of lateral strain. Meanwhile, the growth rate of the compressive volumetric strain continuously decreases to zero at the dilatancy boundary. This marks the onset of damage stage 4, characterized by the dilatancy boundary σ_{cd}. At this point, cracks propagate and merge, forming a major macro-crack at the center of the SEM image (as shown in Fig. 11e). The propagation and interaction of these major cracks become unstable in this damage stage, resulting in an outward deformation of the rock sample in both the axial and lateral directions. As a consequence, the rate of lateral strain growth exceeds that of axial strain, leading to a significant increase in dilatancy. Bieniawski (1967b) concluded that unstable cracks occur after σ_{cd}. And the rate of crack development controls the damage evolution process instead of the external loads. It is worth noting that once the propagation of major macroscopic fracture begins, the initiation of the new short tensile cracks ceases (Hoek and Bieniawski 1965; Li et al. 2018c). The subsequent damage development becomes localized within the region of the major crack, referred to as strain and damage localization (Hao et al. 2007; Jaeger 1979; Rudnicki and Rice 1975).

Through the aforementioned investigation, it is evident that the mechanical response of rocks (such as compressibility and compressive deformation) during the compressive stage (from zero stress to the dilatancy boundary σ_{cd}) follows a dilatancy-resist process. When subjected to compression, the rock undergoes complete compaction through various mechanisms, including microcrack closure, interlocking of irregular crack surfaces, adjustment of mineral grain positions, and elastic deformation of the skeleton. Consequently, both compressive deformation and the dilatancy resistance gradually increase. The crack initiation threshold σ_{ci} marks the onset of the degradation of dilatancy resistance and compressibility in rocks. At σ_{ci}, the volumetric strain curve starts to bend and exhibits a steeper concave shape. Simultaneously, the rate of compressive volumetric strain rate also begins to decrease.

As the dilatancy boundary is approached, the corresponding dilatancy-resist capability of the rock gradually diminishes. Both the compressive volumetric strain rate and dilatancy resistance reach zero at σ_{cd}. If we draw a reference line connecting zero stress and σ_{cd}, the peak point of the "U-shaped" volumetric strain curve corresponds to σ_{ci}.

Based on the mechanisms discussed above, the compressive stage of rock can be divided into two stages (Fig. 10b and c):

1. Stage I: interlocking stage. This stage encompasses the loading period from zero axial stress to σ_{ci}. During this loading period, both the compressive deformation and the dilatancy resistance progressively increase with the applied load. The dilatancy resistance state index curve gradually concaves upward. Correspondingly, in this stage, the value of $|\Delta\delta_{ci}|$ increases from its peak to zero.
2. Stage II: shear sliding stage. This stage consists of the loading period from σ_{ci} to σ_{cd}. In this stage, both the rate of compressive deformation and the dilatancy resistance gradually decrease with the increase in load. Shear sliding occurs during this period, leading to stable initiation of tensile cracks. Due to the relative shear movement along the surface of the pore-like cracks, irregularities or teeth on each shear surface break, collapse, fragment into small fragments, and become lodged in the gaps between cracks. This breaking and rotation of fragments under shear sliding reduce the rock's frictional shear resistance, accelerate the shear sliding between crack surfaces, expedite the loss of dilatancy resistance, and hasten the approach toward dilatancy. Consequently, as shown in Fig. 10b, the dilatancy resistance state curve for stage 2 exhibits a short duration, indicating an accelerated loss of dilatancy resistance. Additionally, in this stage, the value of $|\Delta\delta_{ci}|$ decreases from its peak to 0, corresponding to the shear sliding resistance of the pore-like crack, which also decreases from the maximum to zero. Hence, it can be concluded that $|\Delta\delta_{ci}|$ reflects the dilatancy resistance, influenced by the shear sliding resistance of micropore-like cracks. The $|\Delta\delta_{ci}|$ curve also matches the evolution trend of shear sliding resistance in the crack-like pore. The maximum value of the $|\Delta\delta_{ci}|$ corresponds to the initiation of the dilatancy resistance degradation, indicating the peak growth rate of dilatancy resistance and echoing the corresponding capability of shear sliding resistance in the crack-like pore.

It should be noted that: first, the maximum value of the $|\Delta\delta_{ci}|$ is not equivalent to the internal surface frictional coefficient (i.e., u in Eq. (5)) of the shear sliding crack. The σ_{ci} has the following relationship with coefficient u and σ_3 (Griffith 1924, 1921; McClintock and Walsh 1962):

$$\sigma_{ci} = \frac{(1+u^2)^{1/2}+u}{(1+u^2)^{1/2}-u}\sigma_3 + 4\sigma_t \quad (5)$$

where σ_t is the tensile strength. u is closely related to mineralogy (e.g., mineral particle size, and mineral composition, etc.) and roughness of the crack surface. While the maximum $|\Delta\delta_{ci}|$ is not only related to the mineralogy and roughness of the crack surface but also the normal stress perpendicularly acting on the crack surface.

Second, the shear sliding resistance mentioned in this research only belongs to the crack-like pores in the compressive period. That is to say, the shear sliding resistance is on a microscopic scale, not the macroscopic shear resistance (or strength) of the single shear band. During the compressive period, the tensile cracks generated by the shear sliding effects cracks are isolated from others (Atkinson 2015; Jaeger 1979; Li et al. 2018b; Tapponnier and Brace 1976). Macro-cracks is formed when the deviatoric stress is beyond σ_{cd}. Additionally, the shear sliding is not a disadvantage. It is well known that, compared with tensile strength, rock has higher shear strength, whose value is dozens or even hundreds of times the former. For the samples showing tensile splitting failure characteristics at lower confinement, the tensile cracks generated during the compressive stage fail to connect and interact to form the shear sliding fracture when the deviatoric stress is beyond σ_{cd}. Instead, these tensile cracks extend continuously and propagate parallel to the direction of the axial stress until it runs through the whole sample, leading to the final tensile splitting failure of the sample. In this case, the advantages of the shear strength are not fully utilized, so the bearing capacity of the rock is low. On the contrary, for the samples showing shear sliding failure characteristics, the shear sliding fracture is formed when the deviatoric stress is beyond σ_{cd}, so the rock shows higher bearing capacity and residual strength. This could be the reason that the surrounding rock of the tunnel is easier to collapse by spalling effects, and they still have the bearing capacity even if it is severally shear cracked.

4.3 Validation

This section evaluates the performance of the VSRM utilizing our test data and findings from comparable studies. Table 3 lists the σ_{ci} for Beishan granite (Zhao et al. 2013b). The σ_{ci} of Beishan granite is calculated by the strain-based methods (i.e., VSM, CVSM, LSM, LSRM and the proposed VSRM) and AE method. Table 4 lists the σ_{ci} for Jinyun limestone from our test. σ_{ci} of Jinyun limestone is calculated by the proposed VSRM and the most famous strain-based methods used in Table 3. Furthermore, the mean values of σ_{ci}, standard deviation (SD) and coefficient of variation (CoV) are also presented in Tables 3 and 4.

Tables 3 and 4 show that the σ_{ci} obtained by the strain-based and AE methods are generally consistent, especially for those from the objective strain-based methods (i.e., VSRM, LSRM and CVSM) and the AE method. Thus, the results illustrate that the proposed VSRM can be used to determine the σ_{ci}. The SD varies for these methods, ranging from 2.21 to 5.83 MPa in Table 3 and 1.91 to 6.89 MPa in Table 4. The CoV also varies from 2.15 to 3.72% in Table 3 and 1.19 to 9.38% in Table 4. The variance is due to the subjectivity of the VSM and LSM, which depend on the user's interpretation to plot a tangent line in the lateral strain curve. More concretely, comparing the results of the VSRM and the two subjective methods (VSM and LSM), a large difference comes, especially from the heavily pre-damaged samples, e.g., the samples A-1 to A-5, who are corroded by pH3 acid solution. This is because, as discussed in Sect. 2.2, the linear region of the lateral strain curve of the heavily pre-damaged rock may never genuinely occur during the whole loading process. Therefore, the results from the method using a subjectively plotted linear line may be inaccurate. What's more, there are also some results showing a large difference between VSRM and CVSM (e.g., see samples

Table 3 Summary of σ_{ci} of the Beishan granite obtained by strain-based and AE methods

Sample no.	σ_3/MPa	σ_p/MPa	σ_{ci} obtianed by diffrerent methods (σ_{ci}/MPa)								
			AE	VSM	CVSM	LSM	LSRM	VSRM	mean	SD	CoV/%
BS06MD-01	0	129.61	64.57	60.05	60.42	62.79	64.96	64.69	62.91	2.21	3.52
BS06MD-09	1	160.72	78.94	75.05	77.24	72.55	75.12	77.44	76.06	2.27	2.99
BS06MD-20	5	212.10	88.04	90.15	87.65	92.93	90.90	89.94	89.94	1.94	2.15
BS06MD-25	10	258.27	104.58	100.25	100.05	102.54	109.69	107.24	104.06	3.87	3.72
BS06MD-35	20	311.16	146.94	145.17	140.32	145.42	152.68	150.34	146.81	4.33	2.95
BS06MD-39	30	371.66	157.98	160.65	155.25	155.24	165.843	160.05	159.17	3.99	2.51
BS06MD-40	40	437.17	195.50	183.74	193.93	188.33	198.83	197.62	192.99	5.83	3.02

Note that σ_{ci} and σ_p denote the crack initiation stress and peak strength, respectively. σ_3 is the confining stress ($\sigma_2 = \sigma_3$). Presented data also include the mean values of σ_{ci} (mean), standard deviation (SD) and coefficient of variation (CoV)

Table 4 Summary of σ_{ci} of the Jinyun limestone obtained by different strain-based methods

Solution	Sample no.	σ_3/MPa	σ_p/MPa	σ_{ci} obtianed by diffrerent methods (σ_{ci}/MPa)							
				VSM	CVSM	LSM	LSRM	VSRM	mean	SD	CoV/%
pH 3	A-1	0	86.60	36.51	37.41	32.41	30.45	31.26	33.61	3.15	9.38
	A-2	5	126.34	52.57	50.41	55.54	51.52	52.55	52.52	1.91	3.63
	A-3	10	150.18	50.03	51.41	45.83	47.41	46.95	48.33	2.31	4.79
	A-4	20	175.15	66.53	60.24	68.55	66.45	66.08	65.57	3.14	4.78
	A-5	30	212.08	76.54	70.33	70.05	75.84	76.51	73.86	3.36	4.55
pH 5	B-1	0	90.77	35.52	38.41	40.53	37.51	36.38	37.67	1.94	5.15
	B-2	5	134.46	71.63	70.24	74.72	70.43	71.28	71.66	1.81	2.52
	B-3	10	175.77	73.23	72.24	75.77	72.93	74.48	73.73	1.40	1.90
	B-4	20	180.78	81.52	78.41	83.62	80.51	81.56	81.13	1.89	2.33
	B-5	30	255.21	96.54	92.24	90.00	96.41	96.35	94.31	3.02	3.20
pH 7	C-1	0	120.27	52.36	54.23	55.61	53.41	53.04	53.73	1.25	2.33
	C-2	5	188.03	62.35	60.15	66.61	60.61	62.87	62.52	2.56	4.09
	C-3	10	195.96	78.65	78.81	81.51	77.26	78.89	79.03	1.54	1.95
	C-4	20	233.16	93.54	95.51	90.51	90.02	93.04	92.52	2.27	2.45
	C-5	30	315.24	130.77	125.14	135.51	129.41	130.36	130.24	3.70	2.84
Distilled water	D-1	0	139.07	58.43	50.41	60.61	58.52	55.80	56.75	3.94	6.93
	D-2	5	210.51	70.94	65.41	68.72	75.41	73.74	70.85	3.98	5.61
	D-3	10	252.52	81.93	79.24	80.72	82.41	81.60	81.18	1.25	1.54
	D-4	20	321.37	115.63	110.24	118.62	124.51	127.45	119.29	6.89	5.77
	D-5	30	360.11	140.52	143.41	150.50	146.62	145.65	145.34	3.72	2.56
Dry samples	E-1	0	147.55	55.26	56.42	59.23	59.26	60.71	56.16	0.90	1.60
	E-2	5	216.30	85.44	88.42	88.32	88.31	88.52	87.80	1.32	1.51
	E-3	10	257.50	100.24	103.24	105.42	104.43	105.33	103.73	2.14	2.06
	E-4	20	331.01	130.41	133.50	134.52	133.62	132.40	132.89	1.58	1.19
	E-5	30	370.91	145.85	140.52	145.93	148.53	148.37	145.84	3.24	2.22

Note that σ_{ci} and σ_p denote the crack initiation stress and peak strength, respectively. σ_3 is the confining stress ($\sigma_2 = \sigma_3$). Presented data also include the mean values of σ_{ci} (mean), standard deviation (SD) and coefficient of variation (CoV)

A-1, D-2 and D-3). The elastic parameters (i.e., Young's modulus and Poisson's ratio) have great influence on the determination of σ_{ci}. Therefore, results from the CVSM are uncertain and inaccurate.

In summary, the adoption of the proposed VSRM is highly recommended. Firstly, it offers high objectivity in determining σ_{ci}. This is because the maximum $|\Delta\delta_{ci}|$ and the corresponding σ_{ci} are both unique and easy to be identified, leading to a reduction in subjectivity and inaccuracy. Secondly, it has a simple formula and allows for seamless implementation through programming languages such as Origin, Mathematica, MATLAB, etc. This advantage enables efficient processing of extensive discrete datasets. Thirdly, the VSRM excels in terms of time and cost efficiency. Since stress and strain are readily available and commonly measured data points in rock sample laboratory tests, often monitored through stress and strain gauges, the method proves practical and resource-friendly. Fourthly, unlike the CVSM, the VSRM has high accuracy and is independent of elastic parameters such as E and μ. Lastly, the robust theoretical foundation underlying the VSRM adds further weight to its credibility and utility.

5 Discussions

5.1 Influence of Confinement and Chemical Corrosion on σ_{ci} and $\Delta\delta_{ci}$

According to the investigations in Sect. 4, σ_{ci} occurs at the beginning of the degradation of the dilatancy resistance. This degradation is affected by the shear sliding effects, which are related to the normal stress acting on the crack, crack closure and the strength of the tooth of the crack surface. Chemical dissolution causes damage to rock microstructure,

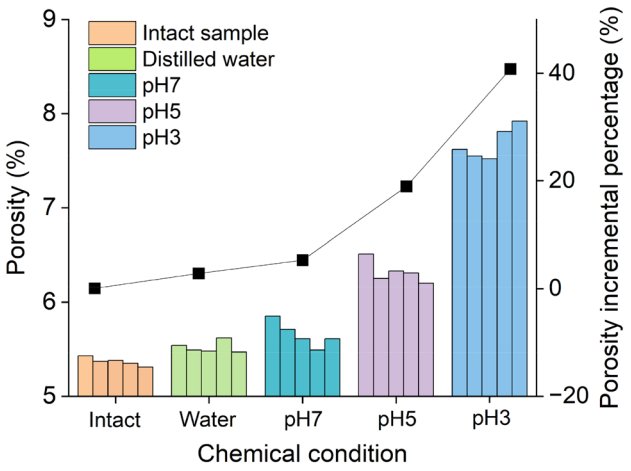

Fig. 12 Change of porosity in limestone samples after 60 days of chemical erosion. The column diagram (left *Y*-axis) shows the porosity of the samples after different chemical treatments. The line and symbol curve diagram (right *Y*-axis) shows the porosity incremental percentage (average value)

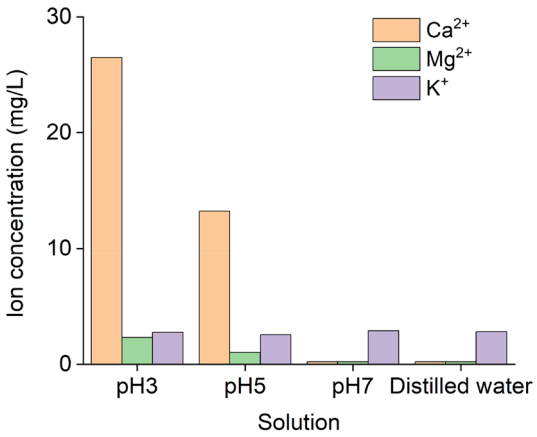

Fig. 13 Ion concentration of the solutions after 60 days of chemical corrosion

e.g., pore size expansion and porosity growth, which may decrease crack closure and the strength of the tooth of the crack surface, then cause deterioration of macro-mechanical properties, e.g., degradations of strength and σ_{ci}.

Figure 12 presents the porosity changes of the samples after 60 days of chemical corrosion. As expect, the samples immersed in pH3 solution have the greatest porosity growth, showing a growth of 37.35%. The water-treated samples have the smallest growth, showing a growth of 4.83%. To analyze the mechanism of pore and crack expansion, it is essential to investigate the ion concentration of the solutions after 60 days of chemical corrosion (see Fig. 13). According to mineral composition analysis, the limestone in this study mainly consists of calcite, dolomite, and feldspar. Two main types of reactions occur: congruent and incongruent dissolution (Brantley et al. 2008). The calcite and dolomite in limestone undergo congruent dissolution in an acidic environment and react with H^+ as follows (Brantley et al. 2008; Jeffery and Hutchison 1981; Stephansson et al. 2004):

$$CaCO_3 + 2H^+ \rightarrow Ca^{2+} + H_2O + CO_2 \uparrow \quad (6)$$

$$CaMg(CO_3)_2 + 4H^+ \rightarrow Ca^{2+} + Mg^{2+} + 2H_2O + 2CO_2 \uparrow \quad (7)$$

The K-feldspar undergoes incongruent dissolution, and kaolinite ($Al_2(Si_2O_5)(OH_4)$) is generated. The reaction formulas are as follows (Brantley et al. 2008; Jeffery and Hutchison 1981; Stephansson et al. 2004):

$$2KAlSi_3O_8 + H_2O + 2H^+ \rightarrow 2K^+ + 4SiO_2 + Al_2(Si_2O_5)(OH_4) \downarrow \quad (8)$$

$$2KAlSi_3O_8 + 3H_2O \rightarrow 2K^+ + 2OH^- + 4SiO_2 + Al_2(Si_2O_5)(OH_4) \downarrow \quad (9)$$

The incongruent dissolution occurs even if the solution is neutral (see Eq. (9)). This is the reason for the porosity growth and mass decrease of the samples in pH 7 solution and distilled water. To quantify the chemical effects (i.e., the chemically induced secondary pore growth) on σ_{ci}, Eq. 10 is introduced as a chemical damage variable D_c (Kachanov 1999):

$$D_c = \frac{n - n_0}{1 - n_0} \quad (10)$$

where n_0 and n is initial porosity and that after chemical corrosion.

Data in Fig. 14a-1 to a-3 come from the limestone samples softened by distilled water and deformed with confining stress of 0, 5, 10, 20 and 30 MPa, showing the influence of the confinement. Data in Fig. 14b-1 and b-3 comes from the samples corroded by different chemical corrosion conditions (i.e., pH 3, pH 5, pH 7 and distilled water) and deformed under the uniaxial compressive condition, showing the influence of the chemical corrosion. From Fig. 14, we observe that confinement and chemical corrosion have two influences: first, they affect the compressive bearing capacity (i.e., σ_{cd}) of the rock. The compressive bearing capacity increase with the increase of confinement and pH value of the chemical solution (see Fig. 14a-1 and b-1). Second, the maximum $\Delta\delta_{ci}$ increases with the increase of confinement and decreases with the increase of chemical damage (see Fig. 14a-2 and b-2). Third, σ_{ci} increases with the increase of confinement and pH value of the chemical solution (see Fig. 14a-3 and b-3).

Higher confining stress not only enhances the fit of the two crack surfaces but also increases the stress perpendicular

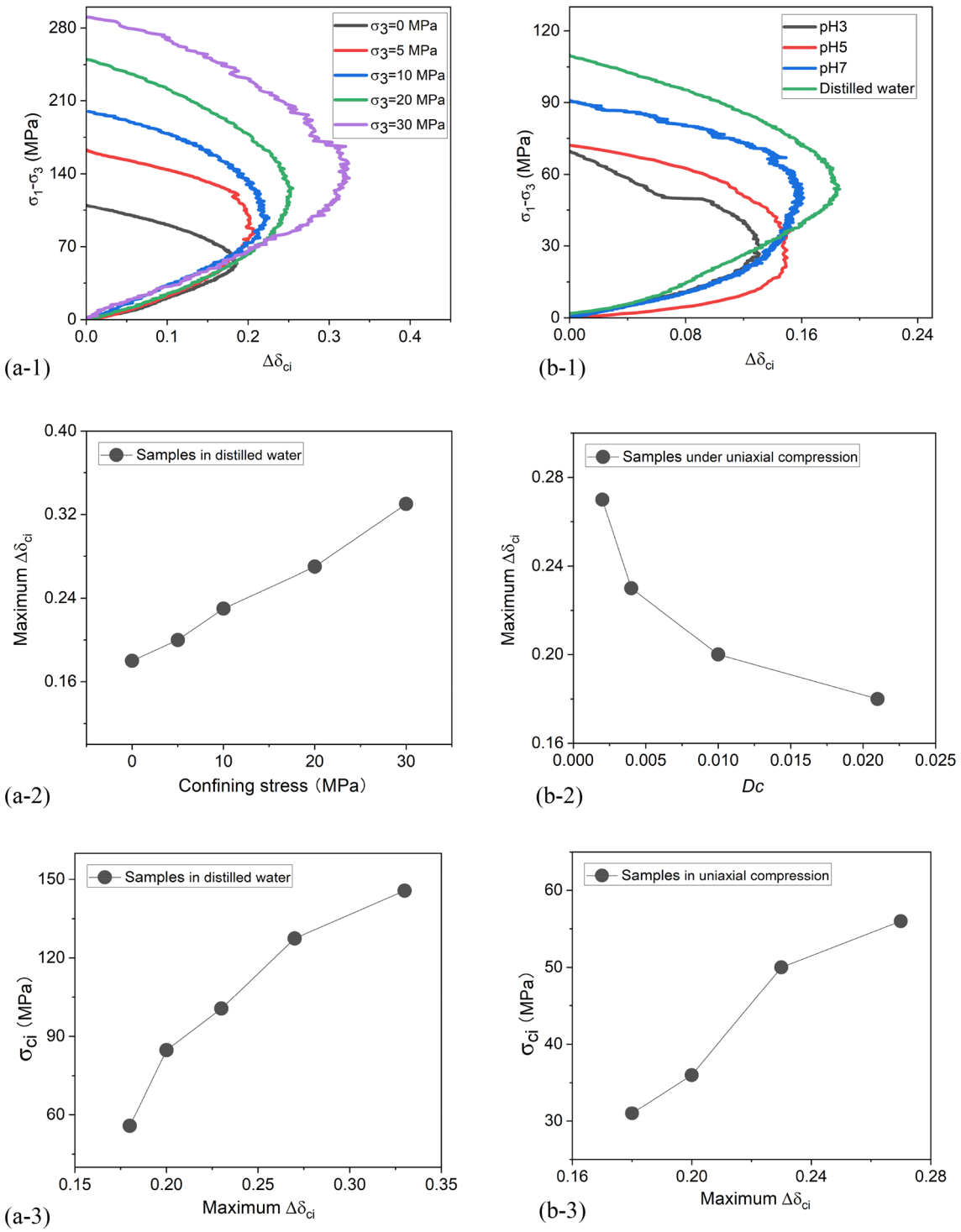

Fig. 14 Influences of chemical corrosion and confinement on σ_{ci} and $\Delta\delta_{ci}$. **a-1** Deviatoric stress ($\sigma_1 - \sigma_3$) versus the dilatancy resistance state index difference ($\Delta\delta_{ci}$) **a-2** Maximum $\Delta\delta_{ci}$ versus confining stress. **a-3** Crack initiation threshold versus maximum $\Delta\delta_{ci}$. Data in **a-1** to **a-3** come from the limestone samples softened by distilled water and deformed with confining stress of 0, 5, 10, 20 and 30 MPa. **b-1** Deviatoric stress ($\sigma_1 - \sigma_3$) versus $\Delta\delta_{ci}$. **b-2** Maximum $\Delta\delta_{ci}$ versus the chemical damage D_c. **b-3** Crack initiation threshold versus maximum $\Delta\delta_{ci}$. Data in **b-1** to **b-3** come from the limestone samples corroded by different chemical conditions (i.e., pH 3, pH 5, pH 7 and distilled water) and deformed under the uniaxial compressive condition

to the shear sliding crack surface. Therefore, the compressive bearing capacity (i.e., σ_{cd}), the peak shear sliding friction resistance (i.e., $\Delta\delta_{ci}$ at the peak point) of the crack-like pore in the compressive stage and σ_{ci} increase with confinement growth. These dissolution processes not only lead to changes in mineralogy and chemical composition but also deteriorate the mechanical properties of limestone samples (Li et al. 2018c), such as the reduction of tooth strength, the diminishment of crack surface roughness, the decrease of both compressive bearing capacity (i.e., σ_{cd}) and peak shear sliding friction resistance of the crack-like pore in the compressive period. Therefore, samples softened by distilled water have higher σ_{ci}, σ_{cd} and maximum shear sliding resistance than those of samples corroded by acid chemical solutions. The sample corroded by pH 3 solution value has the lowest σ_{ci}, σ_{cd} and maximum shear sliding resistance.

5.2 Relations Between the σ_{ci} with Other Rock Mechanical Properties

Section 5.1 presents the effects of confinement and chemical corrosion on σ_{ci}. In this section, we will further investigate the relations between the σ_{ci} with other rock mechanical properties (i.e., Young's modulus, Poisson's ratio, friction angle, cohesion and peak strength). Figure 15a-1 to a-4 present σ_{ci} versus Young's modulus, in which σ_{ci} increases with the Young's modulus. A linear equation can be fitted to describe the relationship between σ_{ci} and Young's modulus. As discussed in Sect. 4.2, when most cracks are closed, elastic deformation takes place, the stress–strain curve becomes linear and the elastic stage starts. In this elastic stage, due to the irregularity of crack surfaces, the crack faces are interlocked caused by external loads so that frictional resistance rises and movement between crack surfaces is restrained. Higher sliding resistance restrains shear sliding and tensile crack initiation, resulting in higher σ_{ci}, lower deformation in stage 2 and higher Young's moduli.

Figure 15b-1 to b-4 show that σ_{ci} is not related to Poisson's ratio. Figure 15c-1 to c-4 and d-1 to d-4 illustrate that σ_{ci} increases approximately linearly with cohesion growth and friction angle loss. As discussed in Sect. 4.2, crack initiation activities are mainly induced by the shear sliding of the pore-like cracks, which is a localized phenomenon (Goodman 1989; Griffith 1924). According to this localized phenomenon, two specific zones can be distinguished: the crack zone and the elastic zone. The crack zone is around the crack-like pore where the tensile crack initiates. The elastic zone is the part that is intact and without crack development. The strength and crack initiation resistance of the elastic zone mainly come from cohesive strength. The larger volume and higher the integrity of the elastic zone, the higher the cohesion will be. The strength and crack initiation resistance of the crack zone mainly come from the frictional resistance strength, which involves the irregularities (teeth) of the crack surface and the normal stress (provided by the rock testing machine) perpendicular to the direction of the shear movement. The crack initiation and development of rock is a process of transforming the elastic zone into the crack zone. Meanwhile, the cohesive strength of the elastic zone is continuously substituted by the frictional resistance strength of the crack zone. Therefore, the larger number and volume of the crack zone, the higher the friction angle will be. When the shear sliding resistance is low, tensile cracks are easy to initiate, the σ_{ci} is lower and more crack zones appear. Therefore, the sample is seriously ruptured by more tensile splitting cracks, showing high friction angle and low cohesion, and vice versa.

Similarly, one can investigate the variation of the σ_{ci} with the peak strength (see Fig. 15e-1 to e-5). Unsurprisingly, σ_{ci} increases with the increase of peak strength. This is because samples with higher Young's modulus and peak strength are more resistant to damage development.

6 Conclusions

A volumetric strain response method (VSRM) is proposed to determine the crack initiation stress threshold (σ_{ci}) of rocks under compression. The VSRM is based on two novel parameters proposed in this paper, i.e., the dilatancy resistance state index (δ_{ci}) and the maximum value of the dilatancy resistance state index difference ($|\Delta\delta_{ci}|$). δ_{ci} represents the state of dilatancy resistance of the rock during the compressive period. While the $\Delta\delta_{ci}$ reflects the evolution of shear sliding resistance of the crack-like pores during the compressive period. The maximum value of the $|\Delta\delta_{ci}|$ corresponds to the beginning of the degradation of the dilatancy resistance and echoes the corresponding maximum capability of shear sliding resistance of the crack-like pore. The volumetric strain curve deflects at the maximum $|\Delta\delta_{ci}|$ and becomes steeper concave upward. The maximum $|\Delta\delta_{ci}|$ divides the compressive stage into two stages, i.e., the interlocking stage and the shear sliding stage. The deviatoric stress corresponding to the maximum $|\Delta\delta_{ci}|$ is taken as the σ_{ci}. The VSRM has been validated by experimental data. Compared to other strain-based methods (i.e., VSM, CVSM, LSM and LSRM), the VSRM is time-and cost-efficient, reduces the user's subjectivity and has an explicit physical meaning, making it capable of processing a large number of discrete data points measured during laboratory testing. Therefore, the VSRM is highly recommended.

The σ_{ci} and maximum $|\Delta\delta_{ci}|$ are affected by the normal stress acting on the crack, crack closure and the strength of the tooth of the crack surface. And they increase with the increase of confining stress and decrease of the secondary porosity induced by chemical corrosion. In terms of the

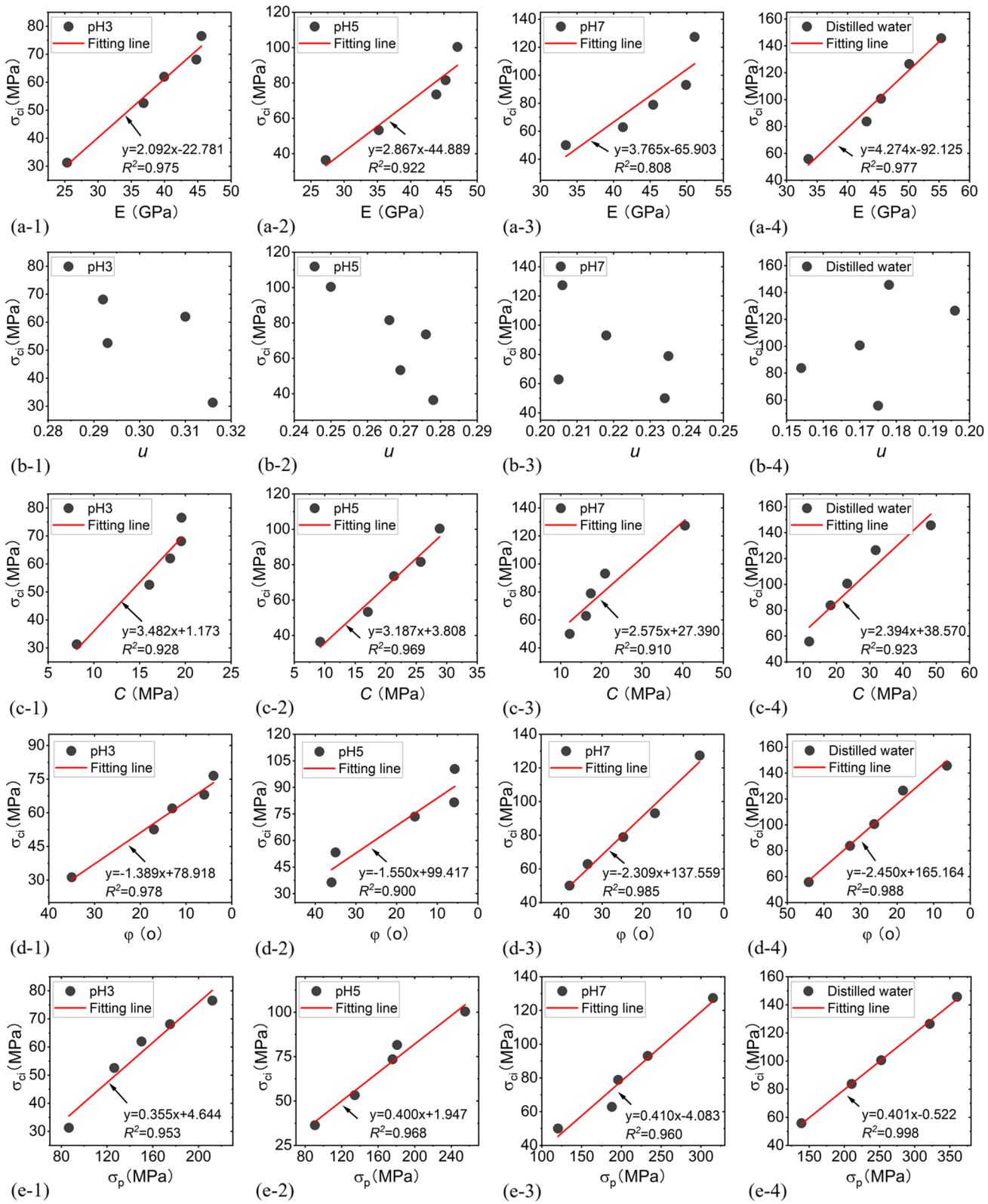

relations between the σ_{ci} and rock's mechanical properties (i.e., Young's modulus, Poisson's ratio, cohesion, friction angle and peak strength), our research shows that the σ_{ci} increases approximately linearly with the increasing Young's modulus, cohesion and peak strength. σ_{ci} decreases

◂**Fig. 15** **a-1** to **a-4** Crack initiation stress threshold (σ_{ci}) versus Young's modulus (E); **b-1** to **b-4** Crack initiation stress threshold (σ_{ci}) versus Poisson's ratio (u); **c-1** to **c-4** Crack initiation stress threshold (σ_{ci}) versus cohesion (c); **d-1** to **d-4** Crack initiation stress threshold (σ_{ci}) versus friction angle (φ); **e-1** to **e-4** Crack initiation stress threshold (σ_{ci}) versus peak strength (σ_p). The four plots in each line (from left to right) show the data of the samples corroded by pH 3, pH 5, and pH 7 acid solution and softened by distilled water, separately. Each plot contains five data points, from left to right, belonging to the samples deformed under constant confining stress of 0 MPa, 5 MPa, 10 MPa, 20 MPa and 30 MPa, separately. Note that **c-1** to **c-4** and **d-1** to **d-4** plot the mobilized cohesion and friction angle at σ_{ci}

approximately linearly with the increase of friction angle. Poisson's ratio does not influence on σ_{ci}.

Recent research by Zhang et al. (2023) shows that the dilatancy boundary of the rocks with pre-existing flaws reaches its peak strength. In contrast, the dilatancy boundary of the intact rock is around 80% of its peak strength. Therefore, future work plans to investigate the applicability of the VSRM on the flawed rocks and the mechanisms of their delayed dilatancy boundary.

Acknowledgements The authors wish to thank Dr. Xiaohong Zhu for useful suggestions and discussion. Special thanks to Prof. Liangqi Zhang and Prof. Keshui Ge for their help, passion and enthusiasm devoted to this scientific investigation.

Funding Open Access funding enabled and organized by CAUL and its Member Institutions.

Data availability Data will be made available on request.

Declaration

Conflict of interest The authors declare that they do not have any commercial or associative interest that represents a conflict of interest in connection with the work submitted.

References

Andersson JC, Martin CD (2009) The Äspö pillar stability experiment: part I—experiment design. Int J Rock Mech Min Sci 46(5):865–878

Andersson JC, Martin CD, Stille H (2009) The Äspö pillar stability experiment: part II—rock mass response to coupled excavation-induced and thermal-induced stresses. Int J Rock Mech Min Sci 46(5):879–895

Atkinson BK (2015) Fracture mechanics of rock. Elsevier

Ben Abdelghani F, Aubertin M, Simon R, Therrien R (2015) Numerical simulations of water flow and contaminants transport near mining wastes disposed in a fractured rock mass. Int J Min Sci Technol 25(1):37–45

Bieniawski Z (1968). Propagation of brittle fracture in rock. In: The 10th US symposium on rock mechanics (USRMS). American Rock Mechanics Association

Bieniawski Z (1967a) Mechanism of brittle fracture of rock: part II—experimental studies. Int J Rock Mech Min Sc Geomech Abstr 4:407–423

Bieniawski ZT (1967b) Mechanism of brittle fracture of rock: part I—theory of the fracture process. Int J Rock Mech Min Sci Geomech Abstr 4:395–406

Brace W, Bombolakis E (1963) A note on brittle crack growth in compression. J Geophys Res 68(12):3709–3713

Brace W, Paulding B Jr, Scholz C (1966) Dilatancy in the fracture of crystalline rocks. J Geophys Res 71(16):3939–3953

Brandtzaeg A, Brown R, Richart F (1928) A study of the failure of concrete under combined compressive stresses. Univ Ill Bull (185): 3–103

Brantley SL, Kubicki JD, White AF (2008) Kinetics of water-rock interaction, 168. Springer, New York

Cai M (2010) Practical estimates of tensile strength and Hoek-Brown strength parameter mi of brittle rocks. Rock Mech Rock Eng 43(2):167–184

Cai M et al (2007) FLAC/PFC coupled numerical simulation of AE in large-scale underground excavations. Int J Rock Mech Min Sci 44(4):550–564

Cannon N, Schulson E, Smith TR, Frost H (1990) Wing cracks and brittle compressive fracture. Acta Metall Mater 38(10):1955–1962

Chang S-H, Lee C-I (2004) Estimation of cracking and damage mechanisms in rock under triaxial compression by moment tensor analysis of acoustic emission. Int J Rock Mech Min Sci 41(7):1069–1086

Chapman DN, Metje N, Stark A (2017) Introduction to tunnel construction. CRC Press, Boca Raton

Cieślik J (2007) Results of triaxial compression tests on LGOM sandstone and dolomite in the context of the elastic-plastic constitutive model selection. Arch Min Sci 52(3):437–451

Cook N (1970) An experiment proving that dilatancy is a pervasive volumetric property of brittle rock loaded to failure. Rock Mech 2(4):181–188

Damjanac B, Fairhurst C (2010) Evidence for a long-term strength threshold in crystalline rock. Rock Mech Rock Eng 43(5):513–531

Diederichs MS (2007) The 2003 Canadian Geotechnical Colloquium: mechanistic interpretation and practical application of damage and spalling prediction criteria for deep tunnelling. Can Geotech J 44(9):1082–1116

Eberhardt E, Stead D, Stimpson B, Read R (1998) Identifying crack initiation and propagation thresholds in brittle rock. Can Geotech J 35(2):222–233

Fan X et al (2018) Internal stress distribution and cracking around flaws and openings of rock block under uniaxial compression: a particle mechanics approach. Comput Geotech 102:28–38

Gao M-B, Li T-B, Meng L-B, Ma C-C, Xing H-L (2018a) Identifying crack initiation stress threshold in brittle rocks using axial strain stiffness characteristics. J Mt Sci 15(6):1371–1382

Gao Y-H et al (2018b) Characteristic stress levels and brittle fracturing of hard rocks subjected to true triaxial compression with low minimum principal stress. Rock Mech Rock Eng 51:3681–3697

Gao Y, Feng X-T, Zhang X, Zhou Y, Zhang Y (2020) Generalized crack damage stress thresholds of hard rocks under true triaxial compression. Acta Geotech 15:565–580
Goodman RE (1989) Introduction to rock mechanics, 2. Wiley, New York
Grgic D (2011) Influence of CO_2 on the long-term chemomechanical behavior of an oolitic limestone. J Geophys Res Solid Earth. https://doi.org/10.1029/2010JB008176
Griffith AA (1921) The phenomena of rupture and flow in solids. Philos Trans Soc Lond A 221(582–593):163–198
Griffith A (1924) The theory of rupture. In: First international congress for applied mechanic, pp. 55–63.
Hao S, Wang H, Xia M, Ke F, Bai Y (2007) Relationship between strain localization and catastrophic rupture. Theor Appl Fract Mech 48(1):41–49
Hem JD (1959) Study and interpretation of the chemical characteristics of natural water. 1473, Reston, VA
Hoek E, Bieniawski Z (1965) Brittle fracture propagation in rock under compression. Int J FractMech 1(3):137–155
Jaeger C (1979) Rock mechanics and engineering. Cambridge University Press, Cambridge
Jeffery PG, Hutchison D (1981) Chemical methods of rock analysis. Pergamon Press Ltd, Oxford
Kachanov LM (1999) Rupture time under creep conditions. Int J Fract 97(1–4):11–18
Lajtai E (1971) A theoretical and experimental evaluation of the Griffith theory of brittle fracture. Tectonophysics 11(2):129–156
Lajtai E (1974) Brittle fracture in compression. Int J Fract 10(4):525–536
Li J, Yue J, Yang Y, Zhan X, Zhao L (2017) Multi-resolution feature fusion model for coal rock burst hazard recognition based on acoustic emission data. Measurement 100:329–336
Li H et al (2018a) A parallel-bonded chemical corrosion model for discrete element modelling of chemically corroded limestone. Eng Fract Mech 202:297–310
Li H, Yang D, Zhong Z, Sheng Y, Liu X (2018b) Experimental investigation on the micro damage evolution of chemical corroded limestone subjected to cyclic loads. Int J Fatigue 113:23–32
Li H, Zhong Z, Liu X, Sheng Y, Yang D (2018c) Micro-damage evolution and macro-mechanical property degradation of limestone due to chemical effects. Int J Rock Mech Min Sci 110:257–265
Liu C et al (2023) Experimental study on failure characteristics of single-sided unloading rock under different intermediate principal stress conditions. Int J Min Sci Technol 33(3):275–287
Lockner D (1993) The role of acoustic emission in the study of rock fracture. Int J Rock Mech Min Sci Geomech Abstr 30:883–899
Lockner DA (1995) Rock failure. Rock physics and phase relations: a handbook of physical constants, vol 3. American Geophysical Union, Washington, DC, pp 127–147
Martin CD (1997) Seventeenth Canadian geotechnical colloquium: the effect of cohesion loss and stress path on brittle rock strength. Can Geotech J 34(5):698–725
Martin C, Chandler N (1994) The progressive fracture of Lac du Bonnet granite. Int J Rock Mech Min Sci Geomech Abstr 31(6):643–659
Martin C, Christiansson R (2009) Estimating the potential for spalling around a deep nuclear waste repository in crystalline rock. Int J Rock Mech Min Sci 46(2):219–228
McClintock F, Walsh J (1962) Fracture in compression of brittle solids. In: Proceedings of the 4th U.S. national congress of applied mechanics, vol 2. American Society of Mechanical Engineers, New York, pp. 1015-1023
Mohr D, Henn S (2007) Calibration of stress-triaxiality dependent crack formation criteria: a new hybrid experimental–numerical method. Exp Mech 47(6):805–820
Moradian Z, Einstein HH, Ballivy G (2016) Detection of cracking levels in brittle rocks by parametric analysis of the acoustic emission signals. Rock Mech Rock Eng 49(3):785–800
Nemat-Nasser S, Horii H (1982) Compression-induced nonplanar crack extension with application to splitting, exfoliation, and rockburst. J Geophys Res Solid Earth 87(B8):6805–6821
Nicksiar M, Martin C (2012) Evaluation of methods for determining crack initiation in compression tests on low-porosity rocks. Rock Mech Rock Eng 45(4):607–617
Nicksiar M, Martin C (2013) Crack initiation stress in low porosity crystalline and sedimentary rocks. Eng Geol 154:64–76
Palchik V (2010) Mechanical behavior of carbonate rocks at crack damage stress equal to uniaxial compressive strength. Rock Mech Rock Eng 43:497–503
Palchik V, Hatzor YH (2002) Crack damage stress as a composite function of porosity and elastic matrix stiffness in dolomites and limestones. Eng Geol 63(3–4):233–245
Peng S, Johnson AM (1972) Crack growth and faulting in cylindrical specimens of chelmsford granite. Int J Rock Mech Min Sci Geomech Abstr 9(1):37–86
Peng J, Rong G, Cai M, Zhou C-B (2015) A model for characterizing crack closure effect of rocks. Eng Geol 189:48–57
Perras MA, Diederichs MS (2016) Predicting excavation damage zone depths in brittle rocks. J Rock Mech Geotech Eng 8(1):60–74
Ranjith P, Jasinge D, Choi S, Mehic M, Shannon B (2010) The effect of CO_2 saturation on mechanical properties of Australian black coal using acoustic emission. Fuel 89(8):2110–2117
Rousseau C-E, Tippur H (2001) Dynamic fracture of compositionally graded materials with cracks along the elastic gradient: experiments and analysis. Mech Mater 33(7):403–421
Rousseau C-E, Tippur HV (2002) Influence of elastic variations on crack initiation in functionally graded glass-filled epoxy. Eng Fract Mech 69(14–16):1679–1693
Rudnicki JW, Rice J (1975) Conditions for the localization of deformation in pressure-sensitive dilatant materials. J Mech Phys Solids 23(6):371–394
Rutqvist J, Tsang C-F (2002) A study of caprock hydromechanical changes associated with CO_2-injection into a brine formation. Environ Geol 42(2):296–305
Sammis C, Ashby M (1986) The failure of brittle porous solids under compressive stress states. Acta Metall 34(3):511–526
Samouëlian A et al (2004) Three-dimensional crack monitoring by electrical resistivity measurement. Eur J Soil Sci 55(4):751–762
Schulson E, Kuehn G, Jones D, Fifolt D (1991) The growth of wing cracks and the brittle compressive failure of ice. Acta Metall Mater 39(11):2651–2655
Singh R (2016) Acoustic emission testing. In: Singh R (ed) Applied welding engineering, 2nd edn. Butterworth-Heinemann, Oxfrd, pp 359–370
Smith A, Dixon N, Meldrum P, Haslam E, Chambers J (2014) Acoustic emission monitoring of a soil slope: comparisons with continuous deformation measurements. Géotech Lett 4(4):255–261
Steinzig M, Ponslet E (2003) Residual stress measurement using the hole drilling method and laser speckle interferometry: part 1. Exp Tech 27(3):43–46
Stephansson O, Hudson J, Jing L (2004) Coupled thermo-hydro-mechanical-chemical processes in geo-systems. Elsevier, Amsterdam
Tapponnier P, Brace W (1976) Development of stress-induced microcracks in Westerly granite. Int J Rock Mech Min Sci Geomech Abstr 13:103–112
Thompson BD, Young RP, Lockner DA (2006) Fracture in Westerly granite under AE feedback and constant strain rate loading: nucleation, quasi-static propagation, and the transition to unstable fracture propagation. Pure Appl Geophys 163(5):995–1019

Tsang CF, Stephansson O, Hudson JA (2000) A discussion of thermo–hydro–mechanical (THM) processes associated with nuclear waste repositories. Int J Rock Mech Min Sci 37(1–2):397–402

Wang Y et al (2014) Research on relationship between crack initiation stress level and brittleness indices for brittle rocks. Chin J Rock Mech Eng 33(2):264–275

Wen T, Liu Y, Yang C, Yi X (2018) A rock damage constitutive model and damage energy dissipation rate analysis for characterising the crack closure effect. Geomech Geoeng 13(1):54–63

Williams PW (2008) The role of the epikarst in karst and cave hydrogeology: a review. Int J Speleol 37(1):1

Wong T-F (1982) Micromechanics of faulting in Westerly granite. Int J Rock Mech Min Sci Geomech Abstr 19:49–64

Xi X, Guo Q, Zhang Y, Pan J, Cai M (2020) Investigating the relationship between the brittleness index and crack initiation stress for the granite under triaxial compression. Latin Am J Solids Struct. https://doi.org/10.1590/1679-78255984

Xu J-M, Liu F, Chen Z-Y, Wu Y-J (2017) Digital features of main constituents in granite during crack initiation and propagation. Eng Geol 225:96–102

Xue L et al (2014) A study on crack damage stress thresholds of different rock types based on uniaxial compression tests. Rock Mech Rock Eng 47:1183–1195

Zhang J-Z, Zhou X-P (2022) Fracture process zone (FPZ) in quasi-brittle materials: review and new insights from flawed granite subjected to uniaxial stress. Eng Fract Mech 274:108795

Zhang Z, Zhang R, Xie H, Liu J, Were P (2015) Differences in the acoustic emission characteristics of rock salt compared with granite and marble during the damage evolution process. Environ Earth Sci 73(11):6987–6999

Zhang R, Yin X, Winterfeld PH, Wu Y-S (2016) A fully coupled thermal-hydrological-mechanical-chemical model for CO_2 geological sequestration. J Nat Gas Scie Eng 28:280–304

Zhang X-P et al (2021) Identifying accurate crack initiation and propagation thresholds in siliceous siltstone and limestone. Rock Mech Rock Eng 54(2):973–980

Zhang J-Z, Zhou X-P, Du Y-H (2023) Cracking behaviors and acoustic emission characteristics in brittle failure of flawed sandstone: a true triaxial experiment investigation. Rock Mech Rock Eng 56(1):167–182

Zhao X, Cai M, Wang J, Ma L (2013a) Damage stress and acoustic emission characteristics of the Beishan granite. Int J Rock Mech Min Sci 64:258–269

Zhao XG, Cai M, Wang J, Ma LK (2013b) Damage stress and acoustic emission characteristics of the Beishan granite. Int J Rock Mech Min Sci 64:258–269

Zhao Z, Shou Y, Zhou X (2023) Microscopic cracking behaviors of rocks under uniaxial compression with microscopic multiphase heterogeneity by deep learning. Int J Min Sci Technol 33:411–422

Zhou X-P, Zhang J-Z (2021) Damage progression and acoustic emission in brittle failure of granite and sandstone. Int J Rock Mech Min Sci 143:104789

Zhou X-P, Zhang J-Z, Qian Q-H, Niu Y (2019) Experimental investigation of progressive cracking processes in granite under uniaxial loading using digital imaging and AE techniques. J Struct Geol 126:129–145